A Novel Single-Cycle Optical Source in the Mid-Infrared

by

Peter Ra Krogen

B.S., University of California Santa Barbara (2012)

S.M., Massachusetts Institute of Technology (2014)

Submitted to the Department of Electrical Engineering and Computer Science

in partial fulfillment of the requirements for the degree of

Doctor of Philisophy Philosophy in Electrical Engineering and Computer Science

at the

MASSACHUSETTS INSTITUTE OF TECHNOLOGY

June 2016

Author . . . .
Department of Electrical Engineering and Computer Science
May 20, 2016

Certified by . . . .
Erich P. Ippen
Elihu Thomson Professor of Electrical Engineering
Professor of Physics
Thesis Supervisor

Certified by . . . .
Franz X. Kaertner
Adjunct Professor of Electrical Engineering and Computer Science
Thesis Supervisor

Accepted by . . . .
Leslie A. Kolodziejski
Professor of Electrical Engineering and Computer Science
Chair of the Committee on Graduate Students

A Novel Single-Cycle Optical Source in the Mid-Infrared

by

Peter Ra Krogen

Submitted to the Department of Electrical Engineering and Computer Science
on May 20, 2016, in partial fulfillment of the
requirements for the degree of
Doctor of Philisophy Philosophy in Electrical Engineering and Computer Science

Abstract

In this thesis, I demonstrate the generation of single-optical-cycle pulses in the mid-infrared, which are generated using adiabatic difference frequency in an aperiodically polled lithium niobate crystal. The input pulses were generated in amplified Ti:Sapphire laser system, the construction of which is covered in detail, along with complete characterization of the generated pulses. The generated pulses have a bandwidth spanning $(1.8 - 4.5\mu m)$, energy in excess of $1\mu J$ at a 1kHz repetition rate, and are compressed to within 15% of their Fourier transform limited duration of 10fs, which is 1.1 optical cycles at their central wavelength of $2.6\mu m$, and represents a peak power well in excess of 100MW. Furthermore, intrinsic to the design of the system is the ability to shape both the spectral amplitude and phase of the generated pulses, which makes this source immediately suitable for applications requiring shaped pulses.

Thesis Supervisor: Erich P. Ippen
Title: Elihu Thomson Professor of Electrical Engineering
Professor of Physics

Thesis Supervisor: Franz X. Kaertner
Title: Adjunct Professor of Electrical Engineering and Computer Science

Acknowledgments

I would like to acknowledge all of those who have helped me along the long journey that has lead me to where I am now. First and foremost, I would like to thank my advisors Professor Franz Kaertner and Erich Ippen, who have provided me an opportunity to pursue my dreams in laser development, and my mentors Jeff Moses and James Fujimoto who have been an invaluable source of skills, guidance, and support. Furthermore, I give my most heartfelt gratitude to my parents who encouraged me to pursue my interests in electrical engineering, and supporting me through the decades of schooling needed to make this all possible. I also must thank all of those who have been involved in construction of the various laser components used in this system, in particular Shu-Wei Huang, Houkun Liang, Koustuban Ravi, Kyung-Han Hong, and Haim Suchowski–it would have been impossible to achieve the results presented here without the years of work put in by my predecessors or the help of my colleagues. Finally, I give my most heartfelt thanks to the love of my life Melissa Johnson, who has always been everything I could ask for.

THIS PAGE INTENTIONALLY LEFT BLANK

Contents

List of Figures

Chapter 1

Preface

The fields of optics, and in particular lasers and nonlinear optics, have been of critical importance in expanding our understanding of the universe. Accordingly, there is an enormously rich history associated with optics, dating back to the the 3rd century BC when the Greek philosopher Euclid noted that light behaves in a fashion consistent with the principals of geometry, which started the field of ray optics. By the 17th century the telescope and microscope had been invented, which made possible the study of objects too small or too far away to be seen by the naked eye–thus beginning the fields of astronomy and microscopy. By the 18th century the wave nature light had been studied, leading to the discovery of diffraction and dispersion, and by the 19th century Maxwell proved that one can derive the behavior of light from the fundamental laws of electromagnetism[46], collectively know as Maxwell's equations which proved to be an exact description of light (and all electromagnetic fields for that matter), so long as the effects of general relativity do not change the properties of the system appreciably, and by the end of the 19th century an improved version of Maxwell's equations had been formulated to take relativistic effects into account. At the turn of the 20th century Einstein proposed that light is composed of discrete wave-packets[3]–and thus started the field of quantum mechanics–and proposed that one could stimulate the emission of light from an atomic system, which is the basis for a laser. The first demonstration of stimulated emission was by Townes in 1953 when he demonstrated the first MASER, which operated at 24 GHz using ammonia as an

active medium[22]. Seven years later the first laser was demonstrated by Maiman at Hughes research labs[45]. Within months Franken, et al. observed the first nonlinear optical effects[19], and 2 years later Armstrong et all[2] put forth a theoretical description of how to solve Maxwell's equations in the case where the medium has a nonlinear response to an incident electric field–thus starting the field of nonlinear optics. Shortly thereafter mode-locking was demonstrated[23], which made possible the study of events too fast to capture with cameras and started the field of ultrafast optics. Within a few years the laser became a workhorse for scientific and industrial applications and made possible countless discoveries, and by the turn of the century lasers had become commodity items. Today virtually every human in the developed world has interacted with a laser in some fashion (if only the laser diode in their CD-ROM drive). Perhaps the most stunning example of the scientific capabilities made possible through laser technology is the recent gravity wave detection made by LIGO–where the displacement of $\approx 4 \times 10^{-18}$ meters between 2 mirrors separated by $4 \times 10^3 m$ (caused by curvature in space-time emitted by the merger of 2 black holes over a billion light years away) was detected using an advanced laser system[44].

One of the many factors that made possible the extreme capabilities and rapid advancement of the fields related to optics is the simple elegance of Maxwell's equations–in a few lines one can *exactly* describe the behavior of electromagnetic fields and waves, as shown in equations 1.1 - 1.5.

$$\nabla \cdot B \quad = \quad 0 \qquad \text{(Gauss's Law)} \tag{1.1}$$

$$\nabla \cdot E \quad = \quad \frac{\rho}{\epsilon} \qquad \text{(Coulomb's Law)} \tag{1.2}$$

$$\nabla \times B \quad = \quad \mu\epsilon\frac{\partial E}{\partial t} + \mu J \qquad \text{(Faraday's Law)} \tag{1.3}$$

$$\nabla \times E \quad = \quad -\frac{\partial B}{\partial t} \qquad \text{(Ampere's Law)} \tag{1.4}$$

Where E and B are the electric and magnetic fields respectively, ϵ and μ are the magnetic permeability electric permitivity of the medium respectively, and ρ is the electric charge density. It is straightforward to show that one solution to these expressions is a propagating electromagnetic wave, with velocity given in expression

12

1.5

$$c = \frac{1}{\sqrt{\mu\epsilon}} \tag{1.5}$$

Of course in vacuum $\epsilon = \epsilon_0$, the permitivity of free space $\approx 8.85 \times 10^{-12} F/m$, and $\mu = \mu_0$, the magnetic constant $4 \times \pi \times 10^{-7} H/m$.

There are caveats of course. For example, as written these expressions are valid only in vacuum and do not take into account relativistic effects or the quantum nature of light; but these limitations not withstanding it is profound that the behavior of light can be exactly solved directly from the fundamental laws of physics. Compare, for example, to Newtonian mechanics whereby the behavior of macroscopic objects are modeled using simple expressions ($F = ma$, etc) which only describe the composite behavior of a complicated system consisting of an ensemble of molecules all interacting through their electromagnetic fields (not to mention relativistic and quantum effects) or the 'law' of supply and demand which attempts to describe the behavior of an incredibly complicated system consisting of intelligent creatures who's behavior is not even deterministic. The governing expressions for optics are absolute, and can often be analytically solved directly with elementary vector calculus, and there exist efficient numerical methods which can solve general systems with arbitrarily high accuracy which can be used for situations which cannot be solved analytically.

Furthermore, extending Maxwell's equations to take into account the effects of a medium (such as the earth's atmosphere, or the glass in an optical system) is relatively straightforward. For nearly all optical systems one can continue to assume that $\mu = \mu_0$, and that the medium has a linear response, so one only needs to calculate ϵ. Unfortunately, in the general case the generated polarization in a material is non instantaneous, which means that ϵ is time varying, and to exactly solve Maxwell's equations one must consider the temporal convolution of the incident electric field with $\epsilon(t)$. However, there are 2 mitigating factors which make this quite manageable. First, calculating $\epsilon(t)$ for a material, at least in concept, is straightforward and can be directly calculated from the quantum-mechanical description of a material (found by solving Schroedinger's equation), or can be directly measured by comparing the

13

propagation of light in a medium relative to vacuum. Furthermore, due to the properties of linear systems, one can write the fields as complex valued phaser fields, and work in the frequency domain by taking the Fourier transform of $E(t)$, $B(t)$, $\epsilon(t)$, etc to get $E(\omega)$, $B(\omega)$, $\epsilon(\omega)$. As a result the convolution in the time domain becomes a frequency domain multiplication and furthermore by considering each frequency component individually, one can solve Maxwell's equations in a linear medium exactly as one would solve them in vacuum by simply setting $\epsilon(\omega)$ to a constant scalar calculated for each frequency component. This works particularly well in many optical systems, because $\epsilon(\omega)$ often varies only slightly with frequency, so it is only necessary to consider a few different optical frequencies to get a good understanding of the effects of a medium in the optical system.

The situation is further complicated when the electric field strength begins to approach that of the inter-atom electric fields, because under these conditions the medium begins to behave in a nonlinear fashion, and as a result its permitivity ϵ varies with the instantaneous electric field in the material. As a result, equations 1.1 - 1.5 become a coupled set of nonlinear differential equations, which in general are not easily solved. However, Armstrong et al. gives an efficient method to solve them, based on two simplifying assumptions[2]. First, one can expand $\epsilon(\omega)$ using a Taylor expansion to get a linear term ϵ, a second order term χ_2 which is dependent on the square of the intensity, a third order term χ_3 dependent on the cube of the intensity, etc. Due to the fact that the nonlinearities in most optical systems are quite small, one can usually consider only the first nonzero term of the Taylor expansion without a significant loss of accuracy. Furthermore, if one assumes that the incident electric field is relatively monochromatic (is is often the case if a laser is used to generate the intense incident field to begin with), with central frequency ω_0 and envelope $\mathcal{E}(t)$ (which varies slowly relative to the carrier frequency), there exists a general solution to Maxwell's equations in a nonlinear medium, which is derived in detail in [2]. The net result of which is that a new propagating field is produced, with central frequency at the sum or difference of the central frequencies of the incident field. Furthermore, energy is transfered between these 2 fields just as energy is coupled between loosely

14

coupled oscillators, as shown in equations 1.6 - 1.8, with a rate determined by the intensity of the incident fields and the nonlinearity in the medium.

$$\frac{\partial \mathcal{E}_1}{\partial z} = -i \frac{\omega_1 d_{eff}}{n_1 c} \mathcal{E}_2' \mathcal{E}_2 e^{-i\Delta kz} \tag{1.6}$$

$$\frac{\partial \mathcal{E}_2}{\partial z} = -i \frac{\omega_2 d_{eff}}{n_2 c} \mathcal{E}_1' \mathcal{E}_1 e^{-i\Delta kz} \tag{1.7}$$

$$\Delta k = (n_2 - n_1)\omega_1 \tag{1.8}$$

Here $\mathcal{E}_1(w)$ and $\mathcal{E}_2(2w)$ are the incident and generated fields, d_{eff} is the relative non-linearity in the material, and n_1 and n_2 are the index of refraction in the material at w and $2w$ respectively. While it can be hard to analytically model the propagation of light in a nonlinear medium directly from Maxwell's equations, it is at least possible to derive the behavior of such a system in just a few lines of calculus with a few simplifying assumptions. Furthermore, there exist many efficient numerical algorithms which can solve the general case of propagation through a nonlinear medium, an example of which is described in detail in chapter 2. An extreme example of this is given in Reference [67], which describes a simulation which solves the general case of broadband few-optical-cycle pulses of light propagating through a medium where the intensity of the incident field is significantly stronger than the intra-atomic fields holding the sub-atomic particles in the medium together, which results in incredibly complex behavior, including the generation of optical pulses in the soft-xray region with pulse durations on the order of 10^{-17} seconds.

Given that the physical laws governing optical systems are so well understood, and that the resulting dynamics can be easily conceptualized, much of the work done in the field of optics today revolves around coming up with new and improved techniques and methods to take advantage of the available optical processes (refraction, interference, nonlinear wave mixing, etc), and solving the practical issues of how to actually build a reliable system which has the desired optical properties. The latter is the focus of the work presented here, which presents an optical system which produces laser pulses in the mid-infrared (central wavelength $2.6\mu m$), with peak intensity well in excess of $100MW$, and pulse durations approximately equal to a single cycle of the optical

carrier wave $(10fs)$. Furthermore, the pulses are generated in such a way that the pulse envelope $\mathcal{E}(t)$ can be arbitrarily shaped under computer control, which make them directly ready for use in a wide variety of experiments.

Chapter 2

Introduction

The terahertz through the mid-IR has long been a 'dark' region for ultrafast coherent sources, with groups pushing from both the lower frequency side through faster transistors and diodes up to nearly 1 THz $(300\mu m)$[69] and from the higher frequency side with optical devices such as quantum cascade lasers[11] and near-IR lasers combined with nonlinear frequency converters such as those based on difference frequency generation (DFG). These sources are typically limited in output power or incredibly complicated/expensive, and it is clear that there is room to improve the state of the art. This has been driven by the fact that the mid-IR wavelength regime is of particular importance to materials science, chemistry, biology and condensed matter physics because it covers a huge number of vibrational absorption bands in biological molecules, solid state compounds, and greenhouse gases. Over the past decade, the improved availability of mid-IR sources with high pulse energies and short durations has made possible a new class of experiments able to probe the most basic properties of molecules and the molecular composition of samples through techniques such as multidimensional spectroscopy[16]. Furthermore, the high peak power and short durations available from these sources have made possible the coherent control of crystal lattice displacements[18] or even individual electron wave packet dynamics on the timescale of their vibrational motion[6] [59], which allows the observation and control of chemical transition states in a sample. At even higher powers it is possible to drive high harmonic generation (HHG) to produce coherent soft x-rays in the water

window [55] and produce self-guided filaments[33][21] with spectral content through the entire UV-VIS-IR-NIR-MIR spectral range.

Furthermore, many of these applications require not only mid-IR sources with high powers and large bandwidths, but they also require precise control over the electric field of the pulse. For example, in nonlinear vibrational spectroscopy, few-femtosecond time resolution and high spectral resolution can be achieved while covering multiple vibrational resonances in multiple functional groups in a sample, but this requires a very flat spectral phase over the entire bandwidth of the pulse and multiple pulse-sequences precisely controlled in timing and relative phase[48]. In high harmonic generation it has been demonstrated that it is possible to tailor the generation of harmonics by using tailored driving fields (typically produced by coherently synthesizing two or more few-cycle optical pulses) in the near-IR and UV to isolate individual harmonics[70] and enhance the harmonic generation efficiency[35]. Furthermore, it has been theorized[29][32] that these techniques can be used in the mid-IR as well to enhance the conversion efficiency to the water-window and even generate isolated attosecond pulses with durations approaching $10as$[13].

There has been a huge amount of progress made over the last decade in the demonstration of novel methods for generating mid-IR ultrafast laser pulses, and a few recent results are summarized in Figure 2-1. Generally, the only methods viable to generate the optical intensities needed for these demanding experiments are based on nonlinear optical effects, either second order effects such as the down-conversion of an ultrafast near-IR laser through difference frequency generation (DFG) or using the idler of an optical parametric amplifier (OPA) or third order effects such as four-wave mixing (FWM) and self phase modulation (SPM) in a plasma. The OPA/DFG sources can be scaled to incredible high powers such as the $\approx 10mJ$ $3.9\mu m$ source[1], however they are typically limited to bandwidths corresponding to several optical cycles in duration due to the phase matching limitations. The sources based on FWM/SPM are able to achieve incredible bandwidths, such the multi-octave-spanning source presented in [52], however these sources are often limited in terms of the quality of the produced pulse (often producing non-Gaussian beams and pulses with pre- and

post- pulses due to residual incompressible spectral phase).

Furthermore, shaping the incredible bandwidths (multi-octave bandwidths are available with FWM approaches) can be quite challenging. Typically such sources would be shaped using a programmable phase element, such as acousto-optic programmable dispersive filter (AOPDF) or spatial light modulator (SLM) inside of a 4-f grating stretcher, however these techniques are generally limited to shaping sub-octave bandwidths. A proposed solution to use these techniques on greater-than-octave spanning pulses is coherent pulse synthesis, whereby multiple laser sources (each of which are shaped, and even possible even amplified) are coherently combined to synthesize a shaped ultrabroadband source. This technique has been demonstrated in a wide variety of experimental configurations[31][71][14], however these systems are generally quite complicated and require very careful attention to the properties of each of the sub-beams to ensure that they all add coherently in a fashion free of jitter,
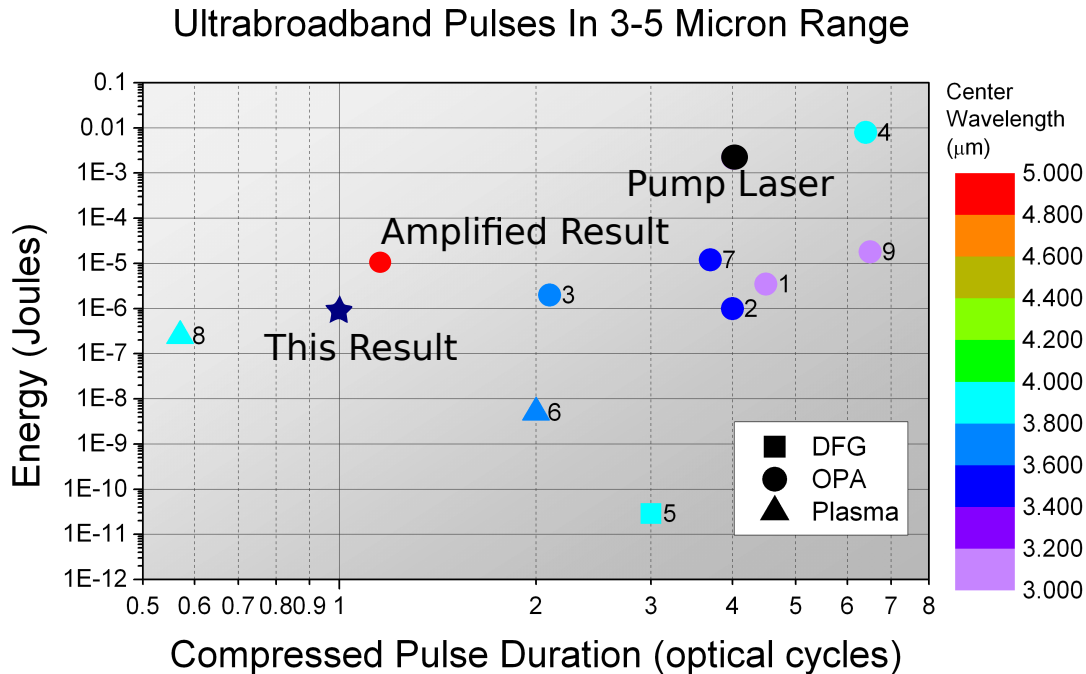
Summary of other mid-IR few-cycle sources, plotted against their energy and measured pulse duration 1 [17] 2 [4] 3 [9] 4 [1] 5 [60] 6 [53] 7 [47] 8 [52] 9 [24]

Figure 2-1: Other Few-Cycle mid-IR Sources

spatio-temporal variations, and drift.

The results presented in this work are based on both DFG and OPA, and can get around the aforementioned limitations to produce an energetic, shaped, greater-than-octave spanning pulse. A key enabling technology used to make this possible is an aperiodically polled $LiNbO_3$ nonlinear grating (the design of which is discussed in detail in Chapter 3) which is capable of efficiently mixing a chirped, broadband near-IR pulse with an unchirped narrow-band near-IR pulse, to generate a broadband chirped mid-IR pulse with greater than octave spanning bandwidth while maintaining a near-unity photon conversion efficiency. This device makes it possible to use traditional chirped-pulse DFG to generate an octave-spanning single-optical-cycle ($10fs$) pulse at $2.6\mu m$ with $1.5\mu J$ pulse energy ($\approx 300MW$ peak power), which has a computer-controlled spectral phase and amplitude, as described in detail in Chapter 6. Such a source has wide applicability for applications requiring ultrabroadband, shaped, mid-IR pulses, as discussed earlier in this chapter.

Additionally, an OPA was constructed to amplify the $3\mu m$ pulse and generate an idler at $6\mu m$ with octave-spanning bandwidth. The idler was confirmed to be sub-two-optical cycles in duration ($\approx 35fs$) at its central wavelength of $6.0\mu m$, with $10\mu J$ pulse energy ($\approx 500MW$ peak power), which is described in detail in Chapter 7. This source was made possible though a new optical material, CSP, and is the first demonstration of octave-spanning parametric amplification in this wavelength region.

Furthermore, several near-IR lasers were constructed to support the mid-IR work, including a chirped-pulse OPA (OPCPA) operating at $2.1\mu m$ with pulse energy of $3.5mJ$ (nearly $1TW$ peak power) and passively carrier-envelope-stable 4-optical-cycle pulse duration ($32fs$), described in Chapter 8. This source was used not only as a pump laser for the $6\mu m$ OPA, but also used to drive high harmonic generation to generate coherent soft X-rays with photon energy up to nearly $500eV$[27][61][61] and for a filamentation study which investigated the nonlinear optical properties of air in the mid-IR[40][40].

Finally, a cryogenic Yb:YAG chirped-pulse laser amplifier generating $50mJ$ $6ps$ pulses ($\approx 15GW$ peak power) at $1030nm$ was also constructed, described in detail in

Chapter 9. This system was used to pump the aforementioned OPCPA system, and to generate intense pulses at $530nm$ and $265nm$[12][25] for near-IR and visible OPCPA pumping, or other tasks requiring picosecond, green/UV pulses such as athermal micromachining. In this system careful attention was taken to ensure that both the short and long term stability of the compressed pulses were sufficient to allow for stable operation of the downstream OPCPA system, which included the addition of feedback loops and careful optical/mechanical design.

THIS PAGE INTENTIONALLY LEFT BLANK

Chapter 3

Adiabatic Difference Frequency Generation

While there are many ways to generate mid-IR laser pulses, as discussed in the intro-
duction, there are relatively few techniques which are capable of generating femtosec-
ond mid-IR pulses, and even fewer techniques capable of generating ultra-broadband
femtosecond mid-IR pulses. One very attractive approach is chirped-pulse differ-
ence frequency generation (CPDFG), which down-converts the broadband output of
a femtosecond near-IR laser to the mid-IR by mixing it with a narrow-band picosec-
ond pulse of light. This technique has a number of advantages, namely that it is
generally significantly easier to generate energetic picosecond pulses of light than
similarly energetic femtosecond pulses, so if one can use a picosecond laser as the
driving source it often gives more freedom when designing the optical system. Fur-
thermore, there is a convenient property specific to chirped-pulse DFG whereby the
spectra phase and amplitude (and accordingly, temporal pulse shape) are transfered
from the near-IR laser to the generated mid-IR pulse. Furthermore, the absolute
bandwidth (the frequency spread) of the near-IR pulse is transfered to the mid-IR,
which has a lower central frequency. This means that the relative bandwidth (the
frequency spread divided by the central frequency) is increased during conversion by
a factor of $\alpha = w_{mir}/w_{nir}$. Alternatively, this can be stated as that the (transform
limited) duration of the near-IR pulse is transfered to the mid-IR pulse, despite the

optical frequency being α times higher. Furthermore, this means that a relatively narrow-band near-IR laser (in this case a pulse spanning $0.65 - 0.83\mu m$, corresponding to a $10fs$ transform limited duration) can be converted to an ultra-broadband mid-IR pulse (in this case a pulse spanning $1.8 - 4.5\mu m$, which also has a $10fs$ transform limited duration). There are of course issues with this approach, both of which becomes harder to solve as the pulse bandwidths increase. First, one must be able to chirp the near-IR pulse and cleanly re-compress the mid-IR pulse. Second, one must locate a suitable nonlinear process to do the down-conversion efficiently. Adiabatic difference frequency generation (ADFG) solves both of these issues.

3.1   Difference Frequency Generation

Difference frequency generation is a subset of the general case of three wave mixing (TWM) in a nonlinear medium with a second order susceptibility. For the general case of TWM, we consider 3 incident electric fields, $\mathcal{E}_1$, $\mathcal{E}_2$, and $\mathcal{E}_3$, with center frequencies ω_1, ω_2, and ω_3 respectively, which satisfy the constraint that $\omega_1 + \omega_2 = \omega_3$. While propagating through a nonlinear medium, these three fields interact through the nonlinearity in the medium, which allows energy to transfer amongst the 3 fields, as described by Equations 3.1-3.4, which can be easily derived from Maxwell's Equations by making a slowly varying envelope approximation as described by Armstrong et al[2].

$$\frac{\partial \mathcal{E}_1}{\partial z} = -i\frac{\omega_1 d_{eff}}{n_1 c}\mathcal{E}_2'\mathcal{E}_3 e^{-i\Delta k z} \tag{3.1}$$

$$\frac{\partial \mathcal{E}_2}{\partial z} = -i\frac{\omega_2 d_{eff}}{n_2 c}\mathcal{E}_1'\mathcal{E}_3 e^{-i\Delta k z} \tag{3.2}$$

$$\frac{\partial \mathcal{E}_3}{\partial z} = -i\frac{\omega_3 d_{eff}}{n_3 c}\mathcal{E}_1\mathcal{E}_2 e^{i\Delta k z} \tag{3.3}$$

$$\Delta k = k_3 - k_2 - k_1 \tag{3.4}$$

Where n_1, n_2, and n_3, are the indices of refraction of the material at each center frequency, c is the speed of light in a vacuum, d_{eff} is the effective magnitude of the second order susceptibility, Δk the phase mismatch (which is a function of wavelength due to the material dispersion), and z is the propagation length through the material.

In the general case (neglecting dispersion of the material) the solution to 3.1-3.4 is a Jacobi Elliptic Integral. An example of this is given in Figure 3-1, which shows a plot of the generated mid-IR wave ($\mathcal{E}_3$) as a function of propagation length through a lithium niobate ($LiNbO_3$) crystal. From this plot one can clearly see a limitation with CPDFG–while it is possible to get unity conversion over a particular wavelength region, there is an inherent trade-off between crystal length (and corresponding conversion efficiency) and the conversion bandwidth. For example, if one selects a 0.05mm thick crystal it is possible to get conversion from $2 - 5\mu m$, but only at less than one percent conversion efficiency. Picking a longer crystal, for example a $0.2mm$ length, gives nearly 80% conversion efficiency, but only over a few hundred nanometer bandwidth.
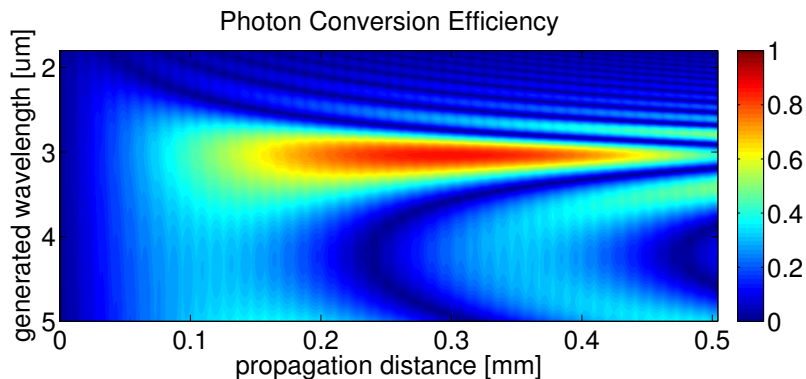
Generated under the same conditions as used to generate Figure 3-3, which were chosen to be similar to those used in the experiment, so as to allow direct comparison between the figures. Nonlinear medium is periodically polled $LiNbO_3$ with a fixed polling period of $30\mu m$. Pump intensity $12GW/cm^2$, seed intensity $1MW/cm^2$, using a flattop seed spectral profile chirped to approximately $3ps$ duration. Note the much shorter crystal length as compared to Figure 3-3.

Figure 3-1: Conversion Efficiency for Constant $\Delta k(z)$

3.2 Adiabatic Difference Frequency Generation

It has long since been known that it is possible to increase the phase matching band-width of a nonlinear optical processes (such as TWM) by varying the phase matching conditions longitudinally in the nonlinear medium, and it was proposed in [5] that it is possible to achieve this in a robust fashion analogous to rapid adiabatic passage.

Specifically in the case where $\mathcal{E}_2$ is strong and undepleted (and thus its derivative is zero) expressions 3.1-3.4 can be reduced to a simpler pair of coupled ordinary differential equations as shown in expressions 3.5 - 3.8.

$$-i\frac{\partial A_1}{\partial z} = \kappa A_3 e^{-i\Delta kz} \tag{3.5}$$

$$-i\frac{\partial A_3}{\partial z} = \kappa' A_1 e^{i\Delta kz} \tag{3.6}$$

$$A_3 = \frac{\mathcal{E}_3}{\sqrt{\kappa}}, A_1 = \frac{\mathcal{E}_1}{\sqrt{\kappa'}} \tag{3.7}$$

$$\kappa = \frac{4\pi\omega_1\omega_2 d_{eff}}{\sqrt{n_1 n_3}c}\mathcal{E}_2 \tag{3.8}$$

which, by no coincidence, possess a SU(2) symmetry and are the same as those that describe nuclear magnetic resonance or the interaction of an electric field with a 2-level atom[7].

$$-i\frac{\partial C_g}{\partial z} = \Omega_0 C_n e^{-i\Delta t} \tag{3.9}$$

$$-i\frac{\partial C_n}{\partial z} = \Omega_0' C_g e^{i\Delta t} \tag{3.10}$$

$$\tag{3.11}$$

This unique case was studied by Suchowski et al[63], who observed that in the case where $\mathcal{E}_2$ is undepleted, it is possible–straightforward even–to make a nonlinear system which exhibits behaviors analogous to rapid adiabatic passage in a 2-level system, and which was later extended to the undepleted case[64]. This is done by observing that

the frequency detuning between the energy of the applied electric field ($\hbar\omega$) and energy level of the absorption ($C_n - C_g$) is related to the phase mismatch in the nonlinear optical system (Δk) and oscillation frequency (Ω) is related to the product of the effective nonlinear coefficient (d_{eff}), the intensity of the applied pump field ($\mathcal{E}_2$) and the material properties, as shown in expressions 3.5 - 3.8. Furthermore, this approach is inherently broadband, and as a consequence of the incredible robustness of adiabatic passage the resulting nonlinear process, adiabatic difference frequency generation (ADFG) is significantly more robust than many other nonlinear optical processes.

An intuitive way to visualize the resulting dynamics is to turn to the Bloch sphere, shown in Figure 3-2, which can be used to represent the transition between 2 quantum states. In this case, one can also use this to visualize the conversion between 2 wavelengths of light, for which a rigorous derivation is given in [63]. The formalism is straightforward–in this case the south pole (w = 0) of the sphere represents the initial state (all photons at ω_3, in the near-IR, ie. no conversion to the mid-IR) and the north pole (w = 1) represents the final state (all photons at ω_1, in the mid-IR, 100% conversion). The U and V axes represent the sum and difference of the cross terms ($E_1 E_3^{'}$ and $E_3^{'} E_1$). Propagation through the nonlinear medium is represented by trajectories on the surface of the sphere, and the projection of any point on the sphere to the w axis directly gives the conversion efficiency. The solutions to Equations 3.6-3.9 are visualized as planes intersecting a sphere, generating a circular trajectory.

To generate a trajectory on the sphere, one draws a vector from the center of the sphere to the starting point (in this case, that is w = 0, which represents the incident near-IR photons), and then rotates about an angle related to the phase mismatch Δk, which generates a circle representing the forward and backward conversion cycles of phase-mismatched difference frequency generation. Two typical trajectories are shown in Figure 3-2a, drawn in orange and blue, and their projection to the w axis are shown in the inset. The blue trajectory shows perfect phase matching, and shows that if the system starts at the south pole (all photons in the near-IR) the conversion efficiency will rise to unity (all photons in the mid-IR) and then cycle back down to the

south pole as back conversion begins to convert the generated mid-IR photons back to the near-IR. The orange trajectory represents the case where there is a nonzero phase mismatch Δk, which has the same general behavior as the blue trajectory representing perfect phase matching, however instead of going through the north pole the conversion efficiency reaches a non-unity maximum (in this case 0.25), and cycles between the near-IR and mid-IR at a faster rate (in the case, it goes through 2 forward/backward conversion cycles for every one cycle of the perfectly phase matched case), as was shown in Figure 3-1.

However, if one carefully varies the phase mismatch over the length of the non-linear medium (in this case by changing the polling period in the $LiNbO_3$ nonlinear grating along its length), the situation changes significantly, as shown in Figure 3-2b. Here the trajectories are no longer limited to circles about a fixed point, but rather spiral around the Bloch sphere and all collect at the north pole. This behavior is fundamentally different than that shown in Figure 3-2a because there is no back conversion, so one can propagate through the nonlinear medium as long as is necessary to get full conversion.

There are of course constraints to achieve this behavior, summarized below, which must be satisfied to achieve efficient, broadband, conversion using ADFG.
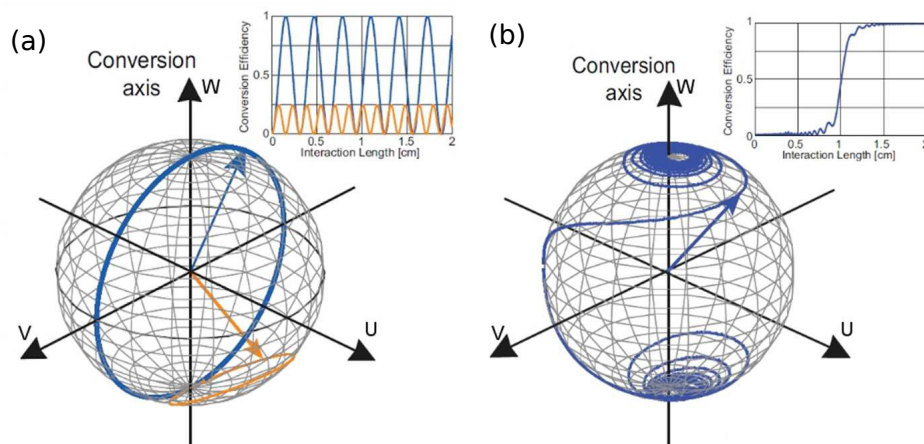
Conversion efficiency plotted for a crystal with constant phase matching conditions (a) and with adiabatically varied phase matching conditions (b)

Figure 3-2: Block Sphere[63]

1. The middle wave E_2 should remain undepleted throughout the interaction

2. The middle wave E_2 should be narrow-band (typically <1 nm of bandwidth)

3. The pulses should be chirped sufficiently that there is not significant temporal walkoff between the different waves

4. The rate at which the phase matching conditions change should be slow

The first 3 constraints are straightforward, and in general these are satisfied by using the chirped-pulse techniques commonly used in high power parametric amplifiers. By chirping the femtosecond near-IR pulse to picosecond duration, and using a narrow-band picosecond pump laser as the pump, the first 3 conditions will be satisfied automatically. Furthermore, the final constraint can be quantitatively described by turning to the Landau-Zener theorem[72], which gives that the conversion efficiency (in this case from the near-IR to the mid-IR) will asymptotically approach unity as the nonlinear coupling κ (related to the pump intensity and material properties, as shown in expression 3.8) is increased and the rate of change of the phase matching conditions is decreased. This allows one to relate the maximum sweep rate of the phase matching conditions (which in turn determines the minimum length of the nonlinear crystal) to κ as shown in expression 3.12.

$$|\frac{\delta \Delta k}{\delta z}| \ll \frac{(\Delta k^2 + \kappa^2)^{3/2}}{\kappa} \tag{3.12}$$

The net result of this being that for a given nonlinear material, and desired pump intensity, one can design an adiabatic converter with an arbitrarily large phase matching bandwidth by selecting a crystal with suitably varied phase matching conditions, and one can place an upper bound on the crystal length required for a given required conversion efficiency. For the device used in this demonstration, it was possible to use a 2-cm long $LiNbO_3$ nonlinear grating to achieve a theoretical 99% conversion efficiency over the $1.4 - 5\mu m$ phase matching window of periodically polled $LiNbO_3$ pumped at $1\mu m$, as shown in Figure 3-3, which shows a simulation of down-conversion of an 800 nm ultrafast laser source to the mid-IR using an adiabatically polled $LiNbO_3$ grating.

The vertical discontinuities come from practical limitations in the discretization of the polling periods used in the device (required so that the device may be physically fabricated) which allow some conversion to occur even when there is a large phase mismatch (a similar phenomenon as the slight conversion which comes are a result of random duty cycle errors). The ripples in the conversion are intrinsic to rapid adiabatic passage (essentially the spirals on the Bloch sphere), however so long as the crystal is long enough that conversion is allowed to complete these are smooth and do not impart significant spectral phase variations to the pulse.
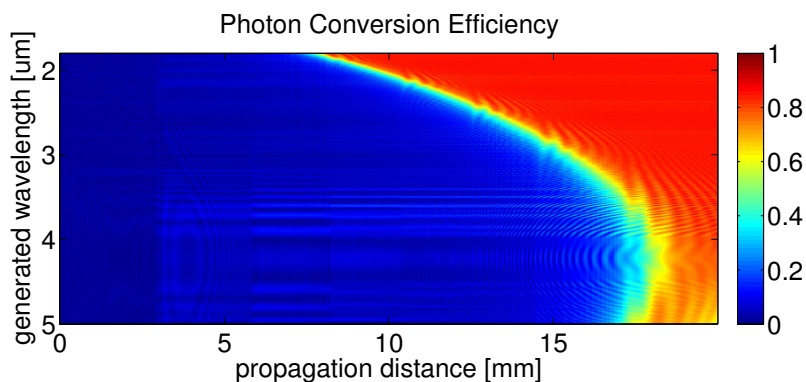
Generated using the pulse propagation simulation described in 4.3, under the same conditions as used to generate Figure 3-1, which were chosen to be similar to those used in the experiment. Pump intensity $12GW/cm^2$, seed intensity $1MW/cm^2$, using a flattop seed spectral profile chirped to approximately $10ps$ duration.

Figure 3-3: Conversion Efficiency for Adiabatically Varied $\Delta k(z)$

Clearly, it is possible to get nearly unity conversion over the entire wavelength region which can be phase matched in the crystal ($1.4 - 5\mu m$, limited by the crystal transparency and practical fabrication limitations). Compare this to Figure 3-1 which shows a simulation under the same conditions but with a constant polling period chosen to give good conversion to the central wavelength of the idler, which achieves good conversion over only a few hundred nanometer bandwidth.

Another useful property of ADFG (and in most other chirped-pulse conversion schemes) is that many of the properties of the seed pulse are transferred to the idler, including the spatial amplitude/phase profiles and spectral amplitude/phase profiles. This means that a pulse shaper operating in the near-IR can be used to shape the

generated mid-IR pulse, which may reduce the complexity of the optical system. In particular, the transfer of spectral amplitude/phase in ADFG is exceptionally useful because the relative bandwidth of the mid-IR idler is much broader than the near-IR signal (CPDFG and ADFG inherently transfer the absolute bandwidth of the signal to the idler, which increases the relative bandwidth by a factor of $\alpha = w_{mir}/w_{nir}$ as defined in Section 3.1. This not only allows one to use a pulse shaper operating in the near-IR to shape the generated mid-IR idler, but also means that the effective bandwidth of the pulse shaper is increased by a factor of α. This property becomes increasingly useful as α and the bandwidth of the generated mid-IR idler becomes broader because pulse shaping schemes become incredibly complex as the shaped bandwidth approaches an octave. Traditional pulse shapers (such as AOPDFs and spatial light modulators inserted into the 4-f stretcher geometry) are incapable of shaping a greater-than-octave spanning bandwidth, however ADFG circumvents this issue entirely by naturally shaping the entire generated bandwidth (which can be octave, or even multi-octave spanning) using an easily shaped few hundred nanometer bandwidth in the near-IR. Furthermore, so long as the pump is relatively narrowband, the spectral features are cleanly transfered to the mid-IR with a simple one-to-one relationship whereby the spectral phase of each near-IR frequency is directly transfered to its corresponding mid-IR frequency ($\omega_{mir} = \omega_{nir} - \omega_{pump}$) with a bandwidth determined by the bandwidth of the pump convolved with the bandwidth of the pulse shaper, and multiplied by α).

THIS PAGE INTENTIONALLY LEFT BLANK

Chapter 4

ADFG Simulation

As with any new technology, it is of critical importance that one not only have a solid theoretical understanding of the technology, but also efficient methods to evaluate potential designs. Luckily, with CPDFG and ADFG the underlying principals governing the conversion process can directly be derived from Maxwell's equations and, as discussed in Chapter 3, can be further simplified to give a manageable analytical model of the process. For this project, 3 different simulations tools were used as needed, including the analytical model shown in Section 4.1, a quasi-monochromatic numerical model shown in Section 4.2, and the full pulse propagation model discussed in Section 4.3.

4.1 Analytical Modeling

The first calculations done related to ADFG were presented in the work done by Suchowski et al[63], where a derivation of the conversion efficiency was given, based on the Landau-Zener theory. The result of this is summarized in expressions 4.1 and 4.2, which states that the conversion efficiency from the near-IR to the mid-IR (or in the case of original work presented in [63] from the mid-IR to the near-IR) can be calculated as a function of material properties, the intensity of the pump wave, and the rate of change of the phase mismatch $\frac{d\Delta k}{dz}$.

$$\Gamma = 1 - e^{\frac{-4\kappa^2}{\pi |\frac{d\Delta k}{dz}|}} \tag{4.1}$$

$$\kappa^2 = \frac{2.232 d_{eff}^2 I_2}{n_1 n_2 n_3 \lambda_1 \lambda_3 c} \tag{4.2}$$

Where d_{eff} is the effective second-order susceptibility in pm/V, I_2 is the pump intensity in MW/cm^2, n_1, n_2, n_3, are signal, pump, and idler indices of refraction; λ_1 and λ_3 are signal and idler wavelengths in cm; c is the speed of light in cm/s; and the sweep rate $\frac{d\Delta k}{dz}$ is in cm^{-2}.

From this result it was possible to confirm that it is possible to get unity conversion efficiency over the greater-than-octave spanning bandwidth $1.4 - 5\mu m$ in a $LiNbO_3$ nonlinear grating with 2-cm length, with a picosecond 1047-nm pump intensity of $10 GW/cm^2$ (well under the damage threshold of $LiNbO_3$), as shown in Figure 4-1.

However, before this device could be considered as a replacement for CPDFG, the chirp imparted in the mid-IR pulse needed to be evaluated to confirm that it is constant against perturbations in the system, smooth, and sufficiently small that it can be removed using available dispersion management techniques. This calculation is in general quite complex, and not easy to solve analytically due to the complicated dynamics of nonlinear pulse propagation through a dispersive media. However, this situation can be simplified by noting that because the near-IR pulse is highly chirped, there is relatively little interaction between adjacent wavelengths. Likewise, one can treat each wavelength pair in the near-IR and mid-IR (related through conservation of energy, where $\omega_{mir} = \omega_{nir} - \omega_{pump}$) separately. Furthermore, for a given wavelength, nearly all of the propagation through the crystal is in a region with a large phase mismatch, so one can treat the nonlinear medium as a simple dispersive linear medium in these regions. The phase imparted in the conversion process itself is approximately constant for all wavelengths (so long as the adiabatic conversion process is not prematurely terminated due to insufficient crystal length), so this phase can be ignored when evaluating the dispersion imparted in the mid-IR pulse. As a result, the spectral phase of the mid-IR pulse can be calculated in a straightforward fashion

34

as a function of the spectral phase of the input near-IR pulse, the crystal's dispersion at the near-IR and mid-IR wavelengths, and the conversion point in the crystal (L) where $\Delta k(\omega) = 0$.

$$\frac{\partial\psi(\omega)_{mir}}{\partial\omega} = \frac{\partial\psi(\omega)_{nir}}{\partial\omega} + k'(\omega_{nir})L(\omega_{nir}) + k'(\omega_{mir})L(\omega_{mir}) \tag{4.3}$$

where $\frac{\partial\psi(\omega)_{mir}}{\partial\omega}$ is the group delay of the generated mid-IR pulse, $\frac{\partial\psi(\omega)_{nir}}{\partial\omega}$ is the group delay if the input near-IR pulse, $k'(\omega)$ is the derivative of the propagation constant, and $L(\omega_{nir})$ and $L(\omega_{mir})$ are the propagation lengths in the crystal at the near-IR and mid-IR wavelengths respectively. This is shown graphically in Figure 4-1 where the the relation between L_{nir} and L_{mir} and the curve along $\Delta k(\omega) = 0$ is overlaid on the conversion efficiency.
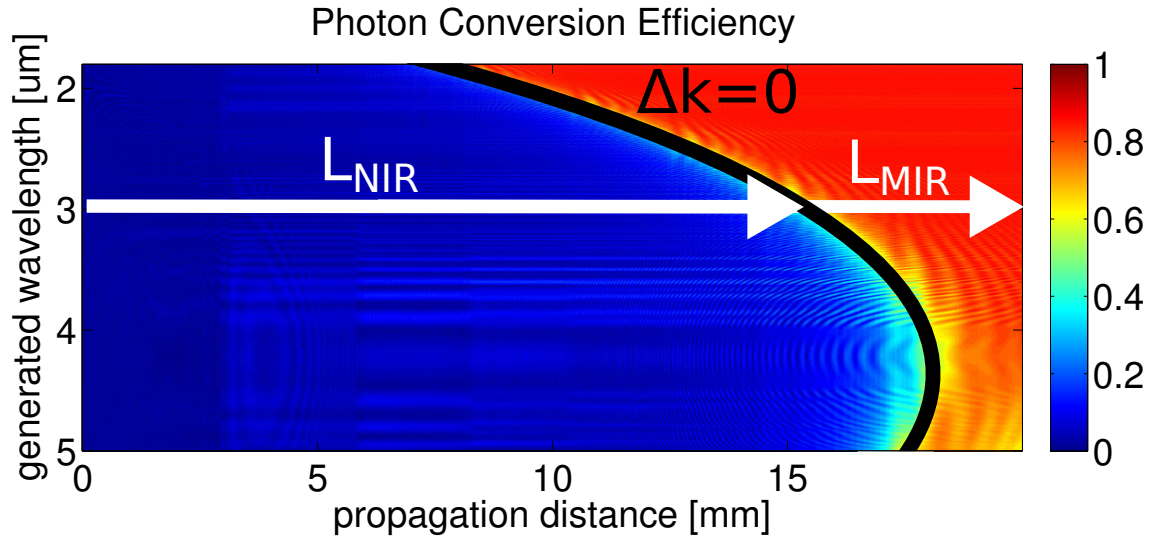
Figure 4-1: Conversion Phase for Varied $\Delta k(z)$

.

So long as the crystal dispersion and phase matching conditions are known analytically, expression 4.3 allows one to calculate the phase on the mid-IR pulse analytically, although when written explicitly it can contain hundreds of coefficients depending on the form of the analytical expressions for the crystal dispersion and phase matching conditions. Nevertheless, they can be solved using computer-aided algebra or using numerical methods, and from this it is possible to extract the expected spectral

phase imparted to the mid-IR pulse. Furthermore, the spectral phase is both smooth and, for the designs discussed here, the group delay is less than $1ps$ so it can easily be compensated in an OPCPA system. Furthermore, we point out that one has a certain degree of freedom to tailor the phase imparted on the mid-IR pulse by changing the rate of change of the phase matching conditions. Because of the asymptotic conversion to the mid-IR, one can locally increase the $\frac{d\Delta k}{dz}$ to affect the dispersive properties of the converter and compensate the reduced conversion efficiency at those wavelengths by increasing the pump intensity.

4.2   Quasi-Monochromatic

While the analytical method proposed in Section 4.1 is elegant, it does have a number of shortcomings. One of which is that it assumes that the phase matching conditions in the adiabatic converter can be varied smoothly–which is not exactly the case in this work. Due to practical limitations when fabricating aperiodically polled devices, the polling periods must be discretized to finite values (typically $0.1\mu m$ which is quite significant relative to the $10\mu m$ half period in these devices), so to achieve a smoothly varying $\frac{d\Delta k}{dz}$ one must dither the polling periods. Due to the discrete nature of this process, it is hard to analytically model the effect of this, although some excellent work has been presented by Phillips, et al.[54] which gives a nice analysis of this and
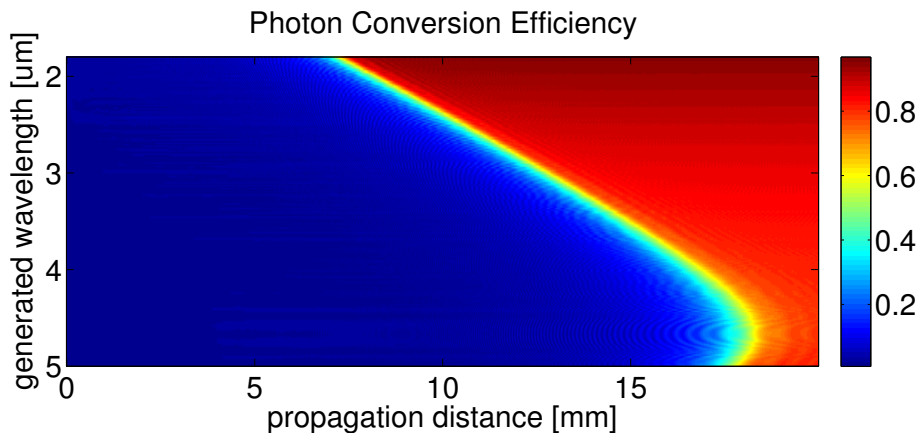

Figure 4-2: Quasi-Monochromatic Simulation

a variety of other parasitic effects in adiabatic conversion that can be encountered in nonlinear gratings and possible techniques to mitigate them. In any case, for this work we elected the straightforward approach of directly integrating expressions 3.1-3.4 using the as-fabricated crystal design to determine the sign of d_{eff} in the integration. The result of a typical simulation is shown in Figure 4.2, which shows the conversion efficiency as a function of wavelength and propagation length in the crystal, evaluated assuming a $12GW/cm^2$ pump intensity.

4.3   Pulse Propagation

Due to the fact that neither the analytical or quasi-monochromatic simulations consider the pulse nature of the ADFG process, it is necessary to turn to a full pulse propagation simulation to evaluate the full ADFG process. Conveniently, due to the asymptotic conversion behavior of ADFG, the entire transverse profile of the near-IR beam can be treated as if it were interacting with a pump beam of constant intensity (even if the pump intensity varies slightly due to its Gaussian profile), and furthermore due to the large size of the beams used in these experiments (roughly $1mm$ diameter) all of the beam can be treated as plane waves. Furthermore, because the conversion is collinear and there is no spatial walkoff (the devices proposed use type-0 phase matching), a simple split step 2-D (1 space and 1 time dimension) simulation is sufficient to accurately model the adiabatic converter. Note - this particular simulation addresses only the sum/difference frequency conversion pathway, and ignores the second harmonic generation and cascaded pathways, and all higher order nonlinearities. This allows accurate calculation of the conversion efficiency and dispersive properties of the sum/difference frequency conversion pathway, but ignores the photons 'lost' due to other conversion pathways. As a result, the actual conversion efficiency is lower than predicted by this simulation, as described in Chapter 5.

This is implemented using a split step method to solve Maxwell's equations by splitting the nonlinear propagation into a linear propagation step (governed by expressions 1.1 - 1.4) and nonlinear conversion step (governed by expressions 3.5 - 3.8).

This simplifies each of the steps to much simpler ordinary differential equation solve 'time step' and multiplication 'frequency step' as shown in expressions 4.4 - 4.12.

Time Domain:

$$\frac{\partial E_1}{\partial z} = -i\frac{\omega_1 d_{eff}}{n_1 c}E_2'E_3 \tag{4.4}$$

$$\frac{\partial E_2}{\partial z} = -i\frac{\omega_2 d_{eff}}{n_2 c}E_1'E_3 \tag{4.5}$$

$$\frac{\partial E_3}{\partial z} = -i\frac{\omega_3 d_{eff}}{n_3 c}E_1 E_2 \tag{4.6}$$

Note: these are identical to the general case presented in expressions 3.1-3.4 with the phase mismatch Δk set to 0. As in the quasi-monochromatic case, these are solved using a 4th-order Runge-Kutta integration.

Frequency Domain:

$$e_1(z + \Delta z) = e_1(z)e^{-ik_1(w)\Delta z}e^{\frac{iw\Delta Z}{V_{frame}}} \tag{4.7}$$

$$e_2(z + \Delta z) = e_2(z)e^{-ik_2(w)\Delta z}e^{\frac{iw\Delta Z}{V_{frame}}} \tag{4.8}$$

$$e_3(z + \Delta z) = e_3(z)e^{-ik_3(w)\Delta z}e^{\frac{iw\Delta Z}{V_{frame}}} \tag{4.9}$$

Note: a retarded frame is used for the propagation, such that the pulse is shifted in time/space to keep it centered within the bounds of the simulation during its propagation. For this simulation the velocity of the retarded frame V_{frame} was selected to be the group velocity of the pump.

Finally, the relationship between the fields is a simple Fourier transform

$$E_1 = \mathcal{F}(e_1) \tag{4.10}$$

$$E_2 = \mathcal{F}(e_2) \tag{4.11}$$

$$E_3 = \mathcal{F}(e_3) \tag{4.12}$$

Due to the broadband and highly chirped nature of the ADFG process, a grid size of roughly 1 million points is needed, and due to the fine pitch of the polling period greater than 10,000 spatial steps are needed. Regardless, acceptable results can be

38
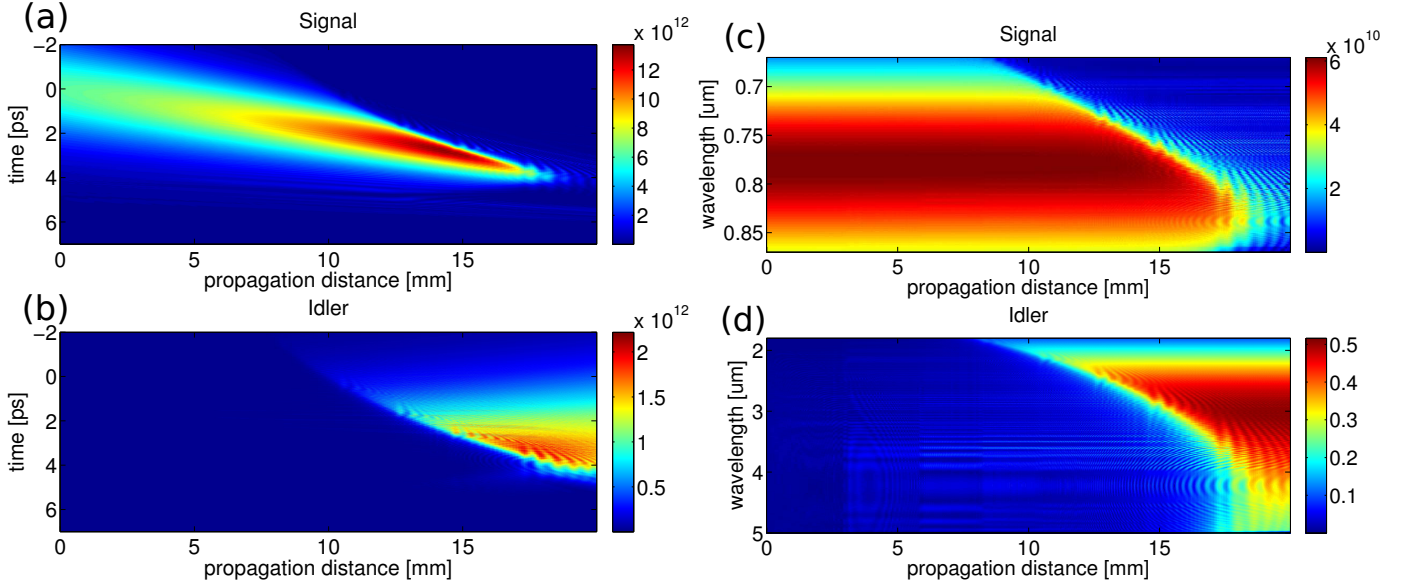
Electric field (a,b in V/m) and Spectrum (c,d in W/Hz) as a function of crystal length, for the near-IR (a,c) and mid-IR (b,d) fields, showing the adiabatic difference frequency generation.

Figure 4-3: Pulse Propagation Simulation

achieved in a 15 minute running time with the code running under MATLAB on an Nvidia GTX580 GPU.

In addition to simulating the nonlinear conversion process, the propagation through the rest of the experimental setup (stretcher, compressor, etc) are considered in the simulation, and provisions are included to evaluate the spectral phase and temporal profile of the pulse throughout the simulated experimental setup.

A simulation of the experimental conditions used for this experiment is shown in Figure 4-3. From this one can observe that there is a significant amount of walkoff between the signal (near-IR) and pump (mid-IR) (the pump is not visible, but has duration $12ps$ and because the simulation is evaluated in the reference frame of the pump it is always centered at time $t = 0$). Furthermore, note that the signal pulse is partially self-compressed as it propagates through the medium. This is a result of the fact that in this demonstration the signal is anomalously chirped, and the ADFG bulk crystal has normal dispersion, so simple linear propagation through the ADFG crystal partially compresses the pulse.

Another key result of this simulation is a highly accurate spectral phase calcula-
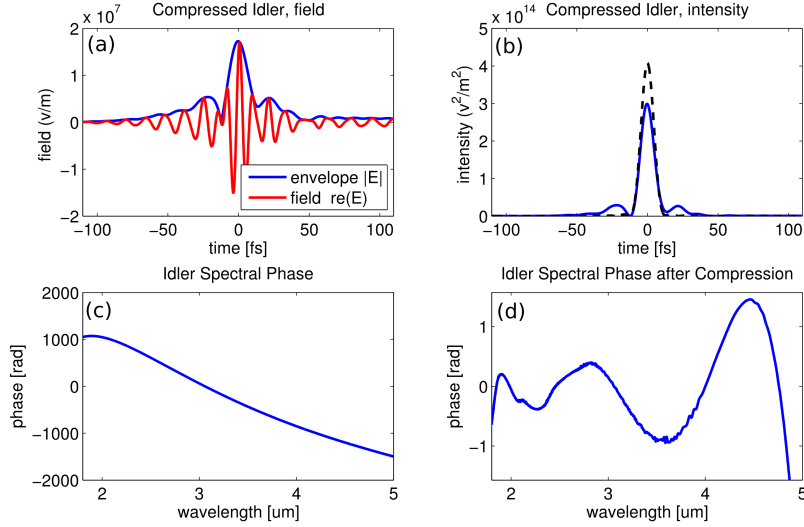
Generated mid-IR idler properties: (a) Compressed idler field, (b, solid) compressed idler intensity, (b,dashed) Fourier limited idler intensity, (c) spectral phase before compression, (d) residual phase after compression

Figure 4-4: Simulated - Compressed Pulse

tion, which includes the effects of the discretized polling period variation, truncated adiabatic conversion process, and varying pump intensity over the duration of the pulse. To evaluate the compressibility of the idler, the simulations were run with a fixed dispersion in the compressor (corresponding to a 20 mm length of silicon), and the dispersion of the input near-IR pulse calculated as the sum of the stretcher dispersion and a 4th order polynomial phase, as might be imparted using the pulse shaper in the experimental setup. Due to the one-to-one spectral phase transfer in ADFG, it was possible to compress the mid-IR pulse by adjusting the spectral phase of the near-IR pulse in just a single iteration. The resulting compressed spectral phase is shown in 4-4, which shows that there is relatively little residual dispersion on the generated mid-IR pulse, and that the pulse is compressed to within roughly 5% of its transform limited duration. The slow ripples in the spectral phase serve to add small wings to the pulse, but peak intensity of the pulse does not suffer significantly, as shown in Figure 4-4b where the simulated pulse is compared to its transform limited equivalent.

Additionally, Figure 4-5 shows a simulation which has a 5-mm thick compressor

(instead of the 20-mm thick one in the previous simulation), and corresponding chirp on the near-IR pulse to give a compressed pulse after the compressor, but with the simulation parameters otherwise unchanged. Due to the much smaller chirp in the near-IR pulse, the near-IR and mid-IR pulses are self-compressed while propagating through the bulk $LiNbO_3$ crystal, and due to the residual 3rd order dispersion the pulses are torn apart. While this does not affect the conversion process, the peak intensities in the crystal are 4 orders of magnitude higher than in the case shown in Figure 4-3, so it is likely that the crystal will be damaged or that unwanted parasitic processes (such as second harmonic generation of the signal or idler, or self phase modulation) will occur at a lower signal intensity. This result demonstrates a potential pitfall associated with this approach, which comes from the fact that due to the long crystal length (20 mm) there is a significant amount of material dispersion, which can cause issues if one is not mindful of it.

This property can be beneficial in fact, and an example of this is the case shown in Figure 4-6. Here the pre-chirp in the near-IR pulse was selected to cause the generated mid-IR idler to be compressed exactly as it exits the adiabatic converter. In this case the adiabatic converter is also used as the compressor, thus eliminating the need to re-compress the pulse entirely. In this configuration the maximum power handling of the device will be significantly limited (the benefits of CPA are lost if the pulse is compressed in the nonlinear medium), however when used as a seed source, or in a high repetition rate system, this may not be a problem. Furthermore, due to the fact that the spectral phase imparted on the mid-IR pulse can be shaped by changing the design of the nonlinear grating, I propose that it would be possible to design an adiabatic converter which accepts a compressed, or nearly compressed, near-IR pulse on the input face of the nonlinear crystal, stretches it through linear propagation through the crystal, converts it to the mid-IR, and then recompresses the pulse all in a single crystal. This could prove to be potential route for an extremely compact mid-IR converter which could be paired with fiber-based femtosecond lasers to generate a compact, high repetition rate, efficient, mid-IR laser source. Furthermore, if both the seed and pump pulses are derived from the same oscillator and amplified in a phase-
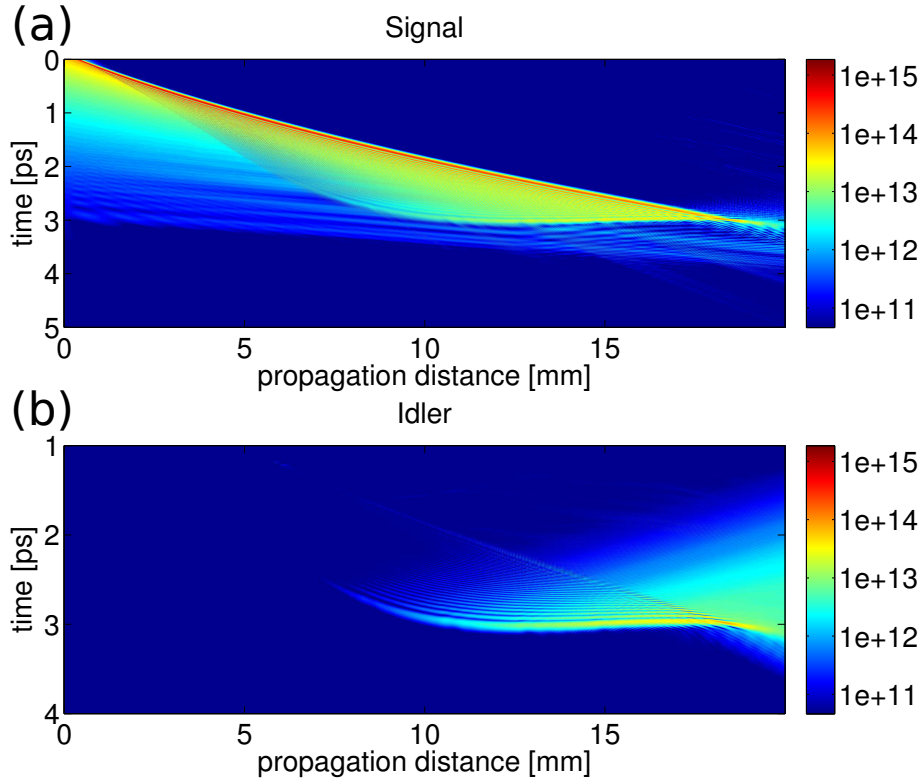
Electric field (a,b in V/m, note the log scale) as a function of crystal length, for the near-IR (a) and mid-IR (b) fields, showing partial self compression of the near-IR signal, followed by adiabatic difference frequency generation. Note that the intensity is plotted on a log scale to better show the highly chirped pulse shape.

Figure 4-5: Simulation - Alternate Compressor

preserving fashion (for example, by amplifying the seed and pump pulses in the same fiber amplifier) the resulting mid-IR pulse would be passively carrier-envelope-stable. Likewise, it would only require stabilization of the repetition rate of the seed laser to generate a frequency comb for spectroscopy applications.
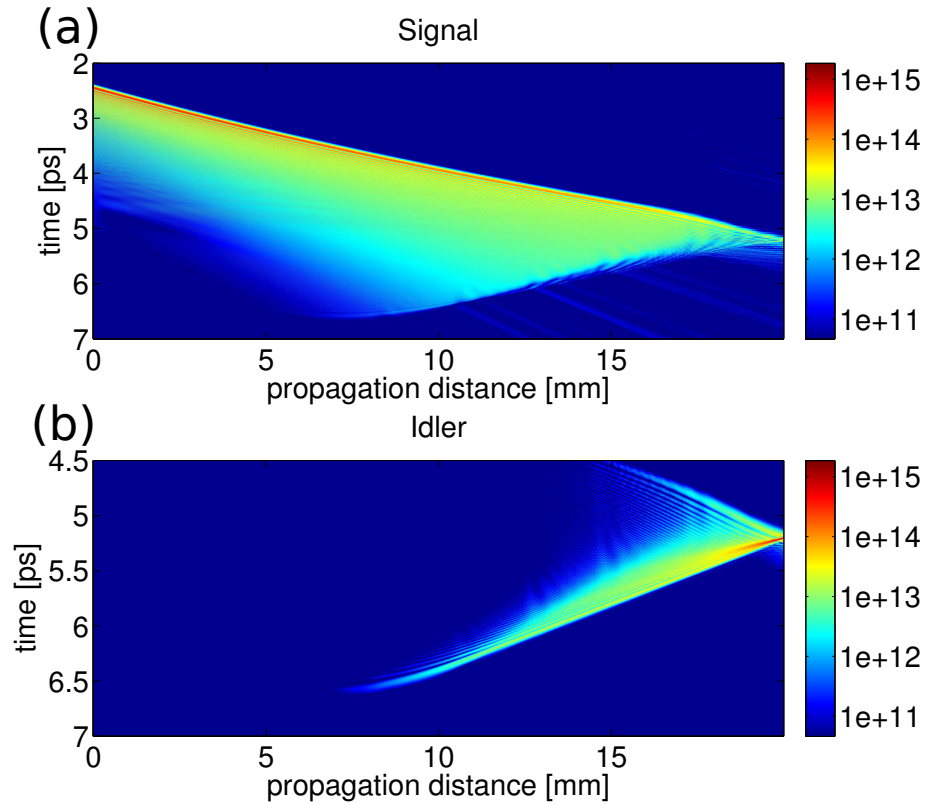
Electric field (a,b in V/m, note the log scale) as a function of crystal length, for the near-IR (a) and mid-IR (b) fields, showing the adiabatic difference frequency generation and compression of the idler. Note that the intensity is plotted on a log scale to better show the highly chirped pulse shape.

Figure 4-6: Simulation - No Compressor

THIS PAGE INTENTIONALLY LEFT BLANK

Chapter 5

Mid-IR Generation Experiments

The adiabatic converter represents only a small portion of the entire optical setup required to generate ultrafast mid-IR pulses using CPDFG. In addition to the ADFG stage, one needs a seed source, stretcher, pump laser, compressor, diagnostic tools to characterize the generated pulses, and possibly additional optical amplifiers, stabilization systems, etc. However, by no coincidence, the adiabatic converter presented here is well suited to be integrated with systems designed for operation with Ti:Sapphire lasers, which are well understood and readily available. Furthermore, the adiabatic converter itself is well within the capabilities of commercial $LiNbO_3$ nonlinear grating manufacturing abilities, so it was possible to have the adiabatic converter used for this demonstration fabricated commercially (HC Photonics).

The situation was further improved because there was an existing custom-built Ti:Sapphire seeded OPCPA system with many of the characteristics needed for these experiments located at MIT. This system was originally a part of the pulse synthesizer demonstrated in [31], and has been described at length [30] [27] [50] [49] [51]. Ultimately this system proved to be unsuitable for use with an adiabatic converter due to limitations related to its bandwidth and stretcher design, however the mode-locked octave spanning Ti:Sapphire oscillator (Menlo Systems Octavius), semi-custom $3.5mJ$, $12ps$, $1047nm$ pump laser[49], and acousto-optical programmable dispersive filter (AOPDF, Fastlite Dazzler), were able to be re-used for this demonstration. An entirely new OPCPA laser system, described in Section 5.1, was constructed for this

demonstration, however we point out that the newly constructed OPCPA can also be used to generate compressed 800-nm pulses (with $10fs$ pulse duration and $30\mu J$ pulse energy) by simply replacing the adiabatic converter and mid-IR compressor with a dispersive glass block (SF9 glass 60 mm in length at Brewster's angle), and adjusting the AOPDF to compensate for the different dispersive conditions.

5.1   Implementation

For this demonstration a 2-stage OPCPA system was constructed, which was capable of delivering highly chirped $30\mu J$ pulses spanning $0.65 - 0.85\mu m$ at repetition rate of $1kHz$, with a controllable spectral phase and amplitude. Figure 5-1 shows the full mid-IR generation system with the details of the OPCPA system shown in the inset.

The OPCPA system consists of 2 non-collinear OPA stages which use BBO as the nonlinear medium. The seed pulses ($\approx 30pJ$ with $6fs$ pulse duration at $800nm$) are first chirped to $\approx 3ps$ in a grating + prism 'grism' pair. They are then amplified in the first stage in a 5 mm thick BBO crystal which uses type I phase matching with $\theta = 24^o$ and non-collinear angle $\alpha = 2.4^o$ in a walkoff compensating geometry, and pumped with $0.25mJ$ $8ps$ pulses at $523nm$ and produces approximately $10\mu J$ pulse energy. This energy is reduced by the combination of another grism pair and AOPDF (Fastlite Dazzler) to $\approx 100nJ$. This is then amplified in the second stage OPA which uses a 2 mm thick BBO crystal using type I phase matching with $\theta = 24^o$, $\alpha = 2.4^o$, in a non-walkoff compensating geometry to reduce parasitic second harmonic generation[10], and pumped with $1.0mJ$ $8ps$ pulses at $523nm$ to produce $30\mu J$ pulse energy. For details on the exact values of dispersion used in the system, see Chapter 6, however for the results shown in Figures 5-2 - 5-4 the chirp was not optimized to compress the generated mid-IR pulse. Rather, the overall dispersion of the stretcher was selected so that the pulse durations in the amplifiers have a good overlap with the pump pulse ($12ps$ in duration) and that the amplified pulse was approximately $3ps$ in duration at the entrance of the adiabatic converter, which was selected to avoid self-compression of the near-IR pulse.
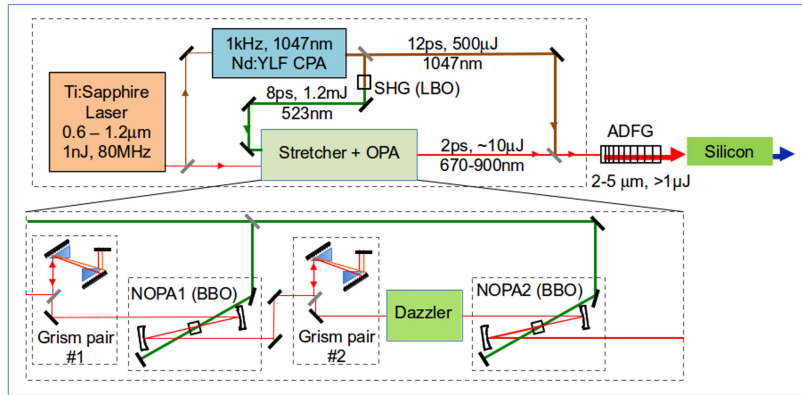
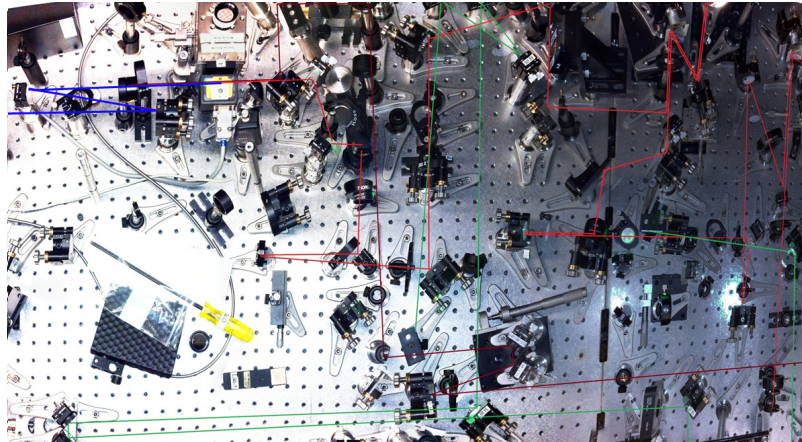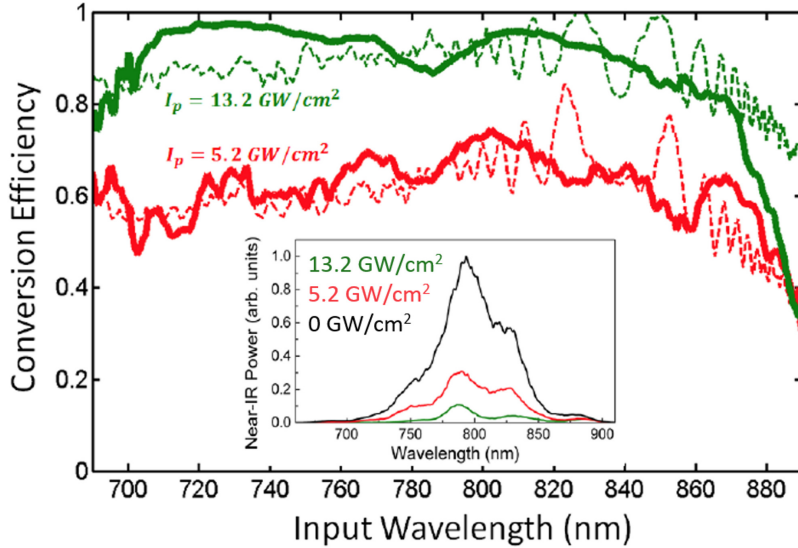Schematic of the ADFG setup[62]

Photo of the ADFG experimental setup. The near-IR beam-line is shown in red, the 523 nm beam-line is shown in green, the 1047 nm beam-line is shown in brown, and the mid-IR beam-line is shown in blue. In operation the system is enclosed in a box purged with dry N2 to avoid atmospheric absorption.

Figure 5-1: ADFG Experimental Setup

Conversion efficiency, as calculated from the near-IR depletion and assuming that all depleted near-IR photons are converted to the mid-IR, plotted against the expected conversion efficiency with a simulated pump intensity approximately 1.6 times higher than the measured pump intensity as the $1.047\mu m$ pump intensity was increased, and the measured near-IR spectra (inset).

Figure 5-2: Near-IR Depletion [31]

5.2   Depletion Measurements

The first experiment performed in the adiabatic converter was a simple measurement of the depletion of the near-IR pulse to confirm that the converter was working as predicted without the complication of measuring the generated mid-IR pulse. The results of this experiment are plotted in Figure 5-2, where spectra of the near-IR pulse (after passing through the adiabatic converter) are shown in the inset. To measure the transmitted near-IR signal a dichroic mirror was used to reject the $1047nm$ pump light, and a grating spectrometer (Ocean Optics USB2000) was used to monitor the near-IR signal. After the spatiotemporal overlap of the pump and signal was experimentally achieved, the intensity of the transmitted near-IR pulses was decreased, a sign that the near-IR photons were being transfered to the mid-IR. By simple conservation of energy one can calculate the apparent conversion efficiency from the near-IR to the mid-IR, which is shown in Figure 5-2 for 2 different pump intensities. Note that even at a relatively low pump intensity of $5 GW/cm^2$, corresponding to a roughly

60% photon conversion efficiency from the near-IR to the mid-IR, the conversion is relatively flat, and matches well with the calculated conversion efficiency based on the simulation results discussed in Chapter 4. This shows that the adiabatic converter is working as predicted, and that the crystal should be suitable for generating compressed mid-IR pulses.

5.3   Generation of Uncompressed Continuum

After the depletion measurements were completed, it was time to move on to measuring the spectrum of the generated mid-IR idler. This is somewhat challenging because the idler is generated collinear to the pump and signal pulses, so a wavelength selective filter is needed to isolate it. Initially a silicon plate was used to absorb the residual pump and idler, however it was discovered that the intense picosecond pulse at 1047 nm was sufficient to cause the silicon to become highly absorbing at the generated mid-IR wavelengths. To combat this, the beam was reflected off of an indium tin oxide (ITO) coated plate, which is highly transmitting at frequencies above its plasma frequency, and highly reflective at frequencies below the plasma frequency [8]. Furthermore, because ITO acts as a resistive metal or lossy dialectic depending on wavelength, it does not significantly chirp the reflected pulse, unlike many dichroic beam splitters. We used a highly conductive ITO coating (deposited by Omega Optical), which was approximately 80% reflecting below 1700 nm and approximately 80% transmitting above 1100 nm. After the majority of the pump beam was transmitted through the ITO filter, it was then possible to use a silicon plate to block out the residual pump and signal. When all of the losses in the system are considered (pump/signal combination, uncoated crystal surfaces, pump/idler separation, and mirror losses) the total throughput of the system is approximately 50%. The resulting mid-IR pulses were characterized using a scanning grating monochromator (Horiba MicroHR) and thermopile power meter (Melles Griot 13SPH003) to measure the spectrum, profile, and power respectively. The spectrum is plotted in Figure 5-3 which shows a bandwidth spanning from $2 - 4.5\mu m$ at 10% of the peak. The
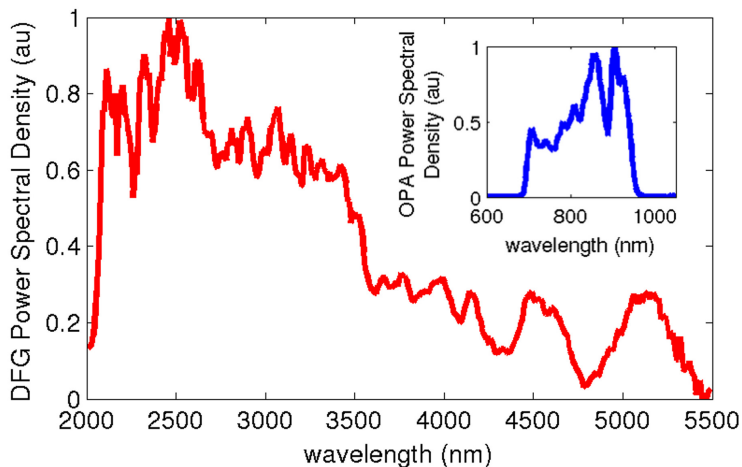
Measured mid-IR spectra spanning $2\mu m - 5.5\mu m$, generated from the near-IR spectra shown in the inset.

Figure 5-3: Uncompressed mid-IR Spectrum

maximum energy achievable in this configuration was $1\mu J$.

5.4 Spectral Amplitude Transfer

To further evaluate the performance of the adiabatic converter, a test was devised to evaluate the transfer of the spectral amplitude of the near-IR to the mid-IR. This was done because it is much easier to measure the spectral amplitude (which can be measured using a simple spectrometer) of a pulse than it is to measure the spectral phase (which requires some sort of interferometric or autocorrelation technique). Furthermore, if the spectral amplitude is transfered as expected it is a good indication (when considered in combination with the depletion measurements discussed in Section 5-2) that the spectral phase is being transfered correctly as well, because it shows that there is little mixing of different signal wavelengths. To evaluate the spectral amplitude transfer, a number of spectral 'holes' were inserted into the near-IR spectrum using the AOPDF in the OPCPA system, and the resulting mid-IR spectrum was measured on a spectrometer. The results of this test are shown in Figure 5-4, which clearly shows that the holes in the near-IR spectral amplitude were transfered to the mid-IR. Furthermore, by comparing the central wavelength of the near-IR holes to

50

those in the mid-IR, and noting that conservation of photon energy implies that a near-IR hole at frequency ω_{nir} should be transfered to a mid-IR hole at frequency $\omega_{mir} = \omega_{nir} - \omega_{pump}$. This was confirmed to be true to within the measurement error of our spectrometers.
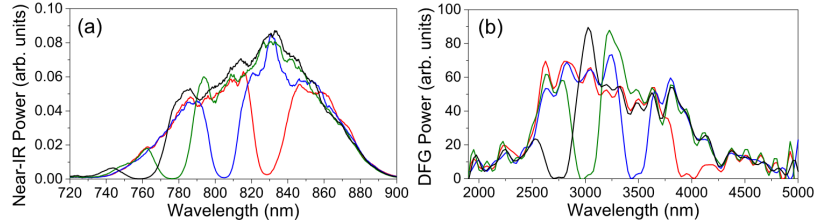

Transfer of the spectral amplitude was confirmed by putting a series of 'holes' in the input spectrum using a Dazzler, plotted in (a), and observed in the mid-IR spectra (b). Note: the slight peaking effect at the edges of the holes is an artifact from the OPCPA system, and is caused by the fact that there is a highly saturated OPCPA after the dazzler. The amplifier is saturated to the point of back conversion in the $760 - 820nm$ wavelength range, so the reduced seed intensity caused by adding a hole causes the amplified signal to increase slightly at the edges of the hole, as can be seen in the near-IR and mid-IR spectra.

Figure 5-4: Spectral Amplitude Transfer [31]

5.5   Spatial Characterization

One additional benefit of ADFG is that, due to the asymptotic dependence of the conversion efficiency on the pump intensity, the spatial profile of the signal can be cleanly transferred to the idler without being shaped by the pump intensity profile. The spatial phase (radius of curvature, beam quality product, etc) will be transfered in any case, but by ensuring that the pump pulse is of sufficient intensity and having a flat spatial phase (a well collimated beam) one would expect that the generated idler will have the same spatial profile as the near-IR signal. This was confirmed by using a pyroelectric camera (Spiricon Pyrocam III) to observe the beam profile of the far-field profile (after the beam was collimated using a f=250 mm curved mirror) the of mid-IR idler. The beam, shown in Figure 5-5, has a clean Gaussian profile which is free of astigmatism, hot-spots, or other issues.
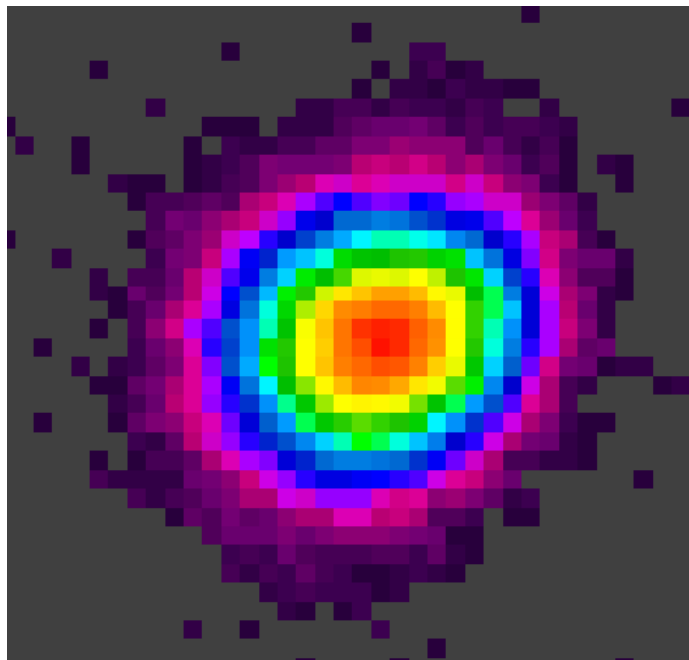
Beam profile of the mid-IR idler (1 pixel = $100\mu m$)

Figure 5-5: Mid-IR Beam Profile

5.6 Absolute Conversion Efficiency

Finally, the absolute conversion efficiency from the near-IR to the mid-IR was measured as a function of signal/idler wavelength. This was done by using the AOPDF to select a $\approx 25nm$ bandwidth in the near-IR and by using a pyrometer (Molectron J3-05) to measure the near-IR and mid-IR energies. The pyrometer has a flat (to within 5%) spectral response over the $0.6 - 6\mu m$ wavelength range needed for this test, so it can be used to measure the relative energy in the near-IR pulse and mid-IR pulse. Additionally, the losses of each of the components in the optical path were characterized so that their losses could be accounted for. The transmission through the adiabatic converter (with no pump applied) was measured to be 70% (this is largely due to reflections from the 2 uncoated crystal surfaces), the reflection of the ITO plate was measured to to be 80%, and the transmission of the anti-reflection coated silicon plate was measured to be 92%, so the total losses in the system come out to 50% from the near-IR measurement point to the mid-IR measurement point, and the internal photon conversion efficiency is calculated as shown in expression 5.1.

$$\gamma = \frac{E_{mir}}{E_{nir}} \times \frac{\lambda_{mir}}{\lambda_{nir}} \times \frac{1}{\beta} \tag{5.1}$$

Where γ is the internal photon conversion efficiency, E_{mir} and E_{nir} are the pulse energy at the mid-IR and near-IR wavelengths respectively, λ_{mir} and λ_{nir} are the wavelengths of the mid-IR and near-IR respectively, and β is the system efficiency as described earlier.

Based on the depletion measurements, one would expect that the conversion efficiency from the near-IR to the mid-IR should be $\approx 90\%$, however this turns out to not be the case. As shown in Figure 5-6, the maximum achievable conversion efficiency is 65% at $2\mu m$ and the conversion efficiency drops off roughly linearly with increasing wavelength down to 15% at $5.2\mu m$. Some of these losses can be accounted for by linear absorption in the system (in particular the dip at $4.2\mu m$ is clearly due to atmospheric CO_2 absorption). It is believed that the remainder of the energy is being converted to a wavelength other than the idler (for example, both the signal

Absolute Conversion Efficiency
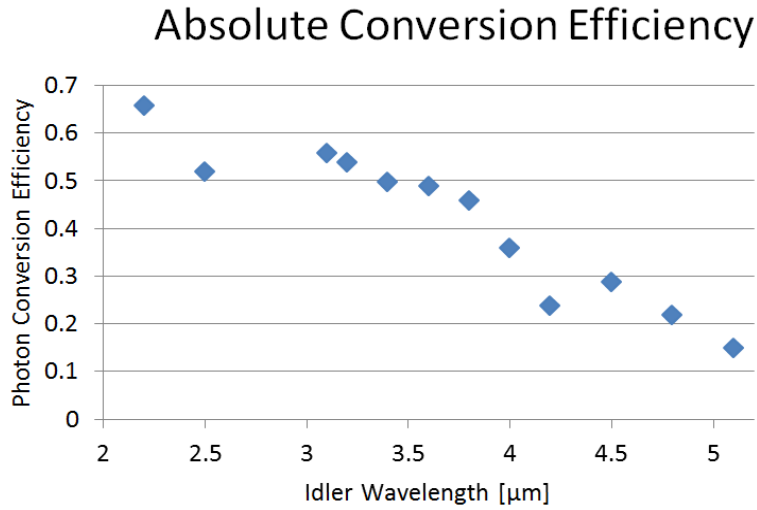
Measured photon number conversion efficiency from near-IR to mid-Ir with a pump intensity of

Figure 5-6: Absolute Conversion Efficiency

and idler can generate their own second harmonic or the signal and pump can mix to generate a sum frequency signal), and this is backed up with spectral measurements showing all 3 of these wave mixing products present. In any case, these issues certainly warrant further investigation through more advanced numerical models and experimental investigation.

Chapter 6

Compression to single cycle duration

The initial compression of the highly chirped pulses generated in an OPCPA system can be challenging due to the large chirps involved in the system. For example, in this demonstration the mid-IR pulse is chirped to approximately 300 times its transform limited duration when it enters the compressor, which is actually a quite modest chirp ratio for an OPCPA system which may have chirp ratios in excess of 10,000[20]. Furthermore, because the duration of the partially compressed pulses is too short to be accurately measured using traditional oscilloscopes, one must turn to autocorrelation or cross-correlation techniques which creates a chicken and the egg situation, whereby the pulse cannot be characterized until it is already nearly compressed. Likewise, it is of critical importance to have a good understanding of the dispersive properties of the optical system so that the pulses can be compressed to within a few times their transform limited duration without any feedback from the experimental setup. It this case, initial compression was achieved by adding the predicted group delay dispersion (GDD) from the adiabatic converter to the calculated GDD of the rest of the components in the optical system (grism pairs, AOPDF, optical crystals, dispersive glasses, etc) to get net GDD of the entire system. Then a suitable length of silicon was selected to re-compress the pulse.

6.1 Initial Compression

To ease the initial compression process the bandwidth of the generated mid-IR pulse was artificially narrowed using the near-IR AOPDF, such that the compressed mid-IR pulses would have a compressed duration of approximately 4 optical cycles. This significantly reduced the dependence of the pulse duration on third- and fourth-order dispersion in the optical system, so the AOPDF could quickly be used to tune the second order dispersion to find optimum compression of the pulses. To evaluate the pulses a home-built second-order balanced interferometric autocorrelator (IAC) was used.

This IAC consisted of 2 50% beam splitters (ISP Optics BSP50-CF-25-2, fabricated on the same run to ensure that they had identical optical properties) selected for low dispersion of both the reflected and transmitted beams, and a home-made piezo-actuated delay line to adjust the delay between the pulses. To generate the second harmonic 2 different nonlinear crystals were used, a $140\mu m$ thick BBO for the $1.8-2.5\mu m$ wavelength range, and a $400\mu m$ thick AGS crystal was used for the $2.5-5\mu m$ wavelength range. An extended InGaAs photodiode (insensitive to the fundamental wavelength) was used for detection, and furthermore a mid-IR polarizer (Edmunds Optics 85262) was used in front of the photodiode to block out any residual fundamental leakage, which is polarized orthogonally to the generated second harmonic. The result of this work is shown in Figure 6-1, which shows interferometric autocorrelations for 3 pulses, centered at $2.2\mu m$, $3.0\mu m$ and $3.8\mu m$ each with a pulse energy of $\approx 1\mu J$. The transform limits of the measured spectra are 26 fs at $2.2\mu m$ (3.4 optical cycles), 41 fs at $3.0\mu m$ (4.0 optical cycles), and 49 fs at $3.8\mu m$ (3.8 optical cycles). The good match between the measured and expected autocorrelation traces shows definitively that there is an insignificant amount of spectral phase variation on the compressed mid-IR pulses, and that pre-chirp imparted on the near-IR signal (experimentally optimized using the DAZZLER by applying a quartic polynomial phase) was sufficient to remove the remaining spectral phase variation on the mid-IR pulse imparted in the adiabatic converter crystal.
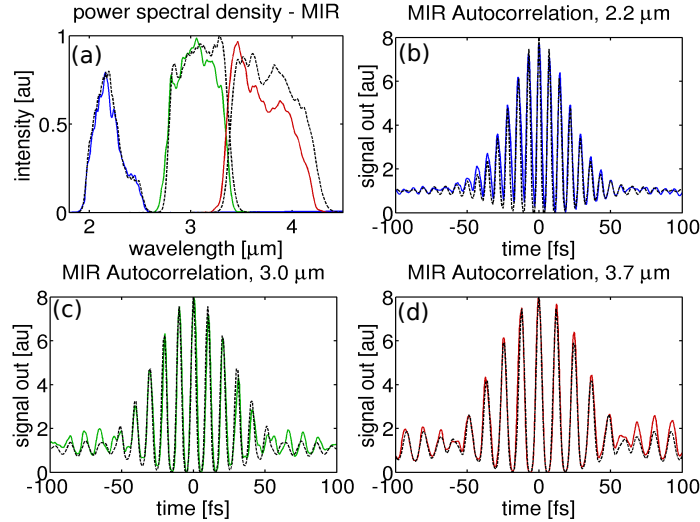
IAC of 4-cycle tunable source, generating a pulse at $2.2\mu m$ (blue), $3.0\mu m$ (green), and $3.8\mu m$ (red), with mid-IR spectra plotted in (a), along with the expected spectrum for each pulse (black), as calculated form the measured near-IR input and assuming 100% photon conversion efficiency to the mid-IR. Additionally, the 3 measured autocorrelations (b-d), each with an overlay (dashed) calculated as the expected autocorrelation, calculated from the mid-IR spectrum and assuming perfect (Fourier-limited) compression, and an ideal second order nonlinearity in the autocorrelator.

Figure 6-1: 4-cycle Tunable Mid-IR Source[37]

We also point out that while this result was a necessary step toward compression of the full bandwidth, the tunable, 4-cycle source demonstrated at this point is a useful tool of its own right. Furthermore, it is tunable using only the AOPDF, and does not require re-alignment of any sort to switch central wavelength, bandwidth, etc. The microjoule energies are sufficient to drive many nonlinear processes, or to seed further amplification stages. In fact this approach was used seed to the parametric amplifier described in Chapter 7. Furthermore, the fact that it was possible to use the near-IR AOPDF to compress the mid-IR pulse conclusively shows that the spectral phase transfer from the near-IR to the mid-IR is working as expected, a result which had not been shown experimentally before this result[37].

6.2 Demonstration of Pulse-Shaping Capability

To further explore the spectral phase transfer, and the utility of this device as a shaped mid-IR laser source, a more advanced pulse characterization tool was constructed, based frequency resolved optical gating (FROG). The IAC discussed in Section 6-1 was converted to operate with a crossed-beam geometry and the photodiode was replaced with a extended InGaAs-based spectrometer (Ocean Optics NIR256) so that the resulting sum frequency signal could be spectrally resolved. Furthermore, to extend the bandwidth available in the mid-IR wavelength region a $140\mu m$ thick AGS crystal was used to generate the second harmonic for pulse pair generation experiments shown in Figure 6-2. To retrieve the resulting spectrograms the code written by J. Wong and provided through the Trebino group was used, which implemented the method of generalized projections as described in [68].

To demonstrate the pulse shaping abilities of the ADFG approach, 3 pulse shapes were selected for measurement. First, a chirp of $2000fs^2$ was imparted on the idler, and the bandwidth was artificially narrowed to 500 nm using the AOPDF. This represents the work shown in Section 6-1 where it was demonstrated that the chirp and bandwidth of the pulse can be shaped. The ability to apply a controlled chirp in the mid-IR idler may seem to be a trivial task, but we point out that this ability is of critical importance when working with ultra-broadband pulses because it allows one to exactly compensate for dispersive optics in the system such as lenses, beam splitters, chamber windows, etc. Second, a pulse pair was generated in the AOPDF with delay of $100fs$ between the pulses, and this pulse pair was transfered to the mid-IR idler. This could be used, for example, when performing pump-probe experiments to impart an extremely precise and drift-free delay between pump and probe pulses. Finally, a pure sinusoidal phase modulation was applied to the idler, which generated a pair of sidebands on the main pulse with total delay of $100fs$ between the lobes. This could be useful in other applications where pulse pairs are needed, such as nonlinear spectroscopy. We point out that there was some amplitude modulation imparted onto the pulse, despite the fact that none was intentionally added. We propose that
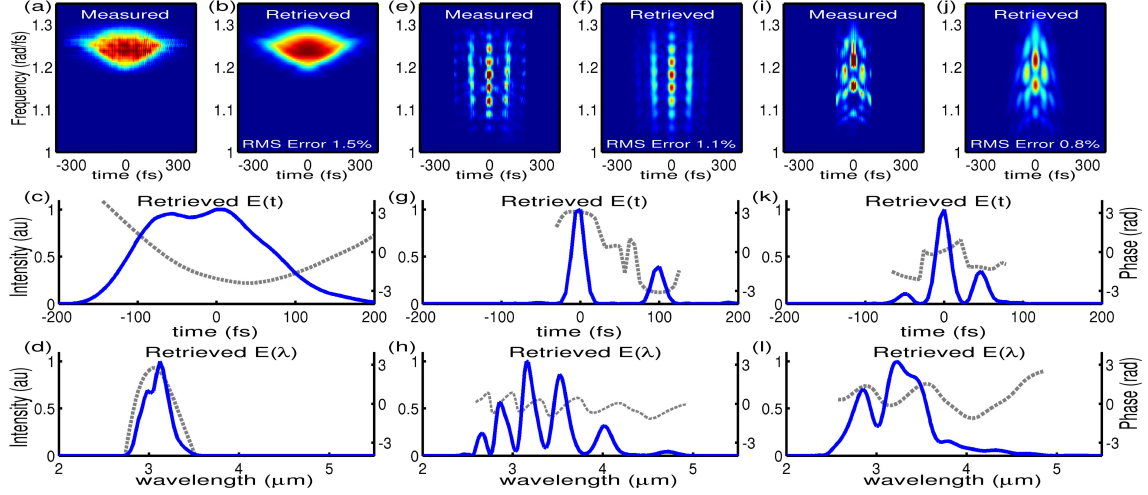
Measured and Retrieved FROG traces (top row), retrieved intensity in the temporal domain (middle row; blue: intensity, gray: phase) and spectral domain (bottom row; blue: intensity, gray: phase), for 3 different input pulses. Left (a-d) linear chirp of $2000 fs^2$, middle(e-h) double pulse with $100 fs$ separation, right (i-l) sinusoidal spectral phase modulation with amplitude of 1 radian and period of 2.00e13 Hz, corresponding to $100 fs$ pulse separation between the generated pulses.

Figure 6-2: Shaped, Few-Cycle Source[36]

this is a result of our OPCPA design, whereby the AOPDF is installed before the second NOPA. This means that if the temporal envelope of the highly chirped ($\approx 3ps$ duration) near-IR pulses changes due to the spectral phase imparted by the AOPDF, saturation effects in the NOPA can convert the phase modulation to an amplitude modulation as seen in these results. This can of course be avoided by moving the pulse shaper directly before the adiabatic converter, but we point out that in applications where this is an issue it is possible to simply use the amplitude shaping abilities of the AOPDF to pre-compensate for the phase-to-amplitude coupling in the amplifier to flatten out the generated spectrum.

6.3 Compression to Single-Cycle Duration

After having fully characterized the adiabatic converter, the only task left was to compress the full bandwidth of the pulse. Due to the ultra-broadband nature of the generated mid-IR idler (spanning nearly 1.3 octaves at -10 dB from the peak)

the compression of the idler required very careful attention to detail. For example, propagating through 1 mm of CaF_2 chirps the pulse from transform limited to approximately 5 times its transform limited duration. Propagating though 1 mm sapphire (a commonly used mid-IR transparent optical material) chirps to the pulse to 50 times its transform limited duration.

First, the pulse characterization system needed to be improved, because the phase matching bandwidth of the $160\mu m$ thick AGS crystal (as thin as could be commercially manufactured at the time) was too small to support second harmonic generation of the full pulse. Several methods to mitigate this issue were considered (crystal angle dithering, switching to a third harmonic or sum frequency nonlinearities, etc) but ultimately we decided to stick with SHG-FROG but switch to GaSe as the nonlinear medium. GaSe was selected because it can be cleaved as thin as $10\mu m$ thick, has very broad phase matching in the mid-IR, and a nonlinear coefficient several times higher than that of AGS. Based on traditional phase matching calculations it was concluded that a readily available $30\mu m$ thick GaSe crystal would be able to generate second harmonic of the entire bandwidth of the idler simultaneously. There is one drawback to using GaSe, which is that it is only commercially available when cut at $\theta = 0$ and cannot be periodically polled or temperature turned appreciably. However, as luck would have it, it is possible to angle tune the whole crystal to get phase matching from $10\mu m$ down to approximately $1.5\mu m$ before phase matching becomes geometrically impossible. For this work the GaSe crystal was used at $\Theta = 38^o$ (external angle), which corresponds to fundamental central wavelength of $3\mu m$[66]. One downside to this approach is that the for type I SHG the polarizations are such that the Fresnel reflection of the fundamental wavelength off of the uncoated crystal surface is approximately 50%, but this is a small price to pay for the incredibly broad phase matching bandwidth, transparency window, and the ability to get freestanding crystals as thin as $10\mu m$ thick.

With the $30\mu m$ thick GaSe crystal installed in the autocorrelator it was possible to characterize the full bandwidth of the generated mid-IR pulse at once, so work could start on compressing the pulse. Using the compression results from the initial
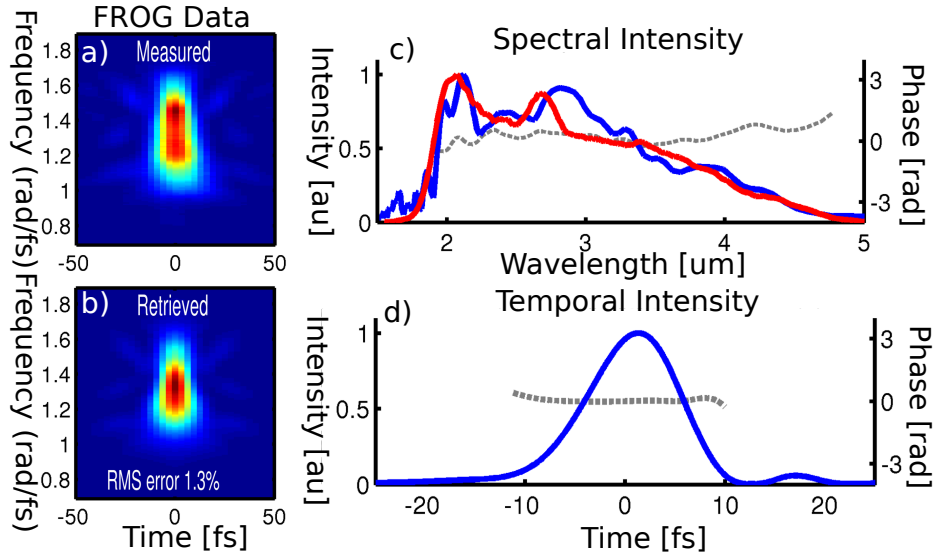
(a-b) Measured and Retrieved FROG traces of single cycle mid-IR pulse. (c) Retrieved intensity in the temporal domain (top right; blue: retrieved intensity, red: measured intensity, gray: phase). (d) Retrieved temporal intensity (blue: retrieved intensity, gray: phase).

Figure 6-3: Single-Cycle Source

compression experiments as a starting point, the chirp in the mid-IR pulse was iteratively modified by characterizing the phase using FROG and then modifying the programmed dispersion in the AOPDF to minimize the residual phase. A simple Newton's method was used to remove the error. To reduce the noise in the system, instead of directly optimizing the spectral phase $\phi(wt)$ on a point by point basis, the spectral phase was fit to a polynomial and this polynomial used to generate the new dispersion. A 4th order polynomial was sufficient to compress the pulse down to roughly 1.5 cycle bandwidth, but ultimately an 8th order polynomial was used to compress the full bandwidth. While it is unlikely that an 8th order polynomial was actually necessary, there was little drawback to adding additional terms in the fitting so this was selected to give the best possible compression without letting noise get into the system.

Ultimately, it was possible to compress the pulse to within the measurement error in our system, which corresponds to a pulse which is approximately 15% longer than its transform limited duration of $10fs$, as shown in Figure 6-3. This corresponds to 1.1 optical cycles at its central wavelength of $2.6\mu m$. Furthermore, with improvements

made to the optical system (general alignment optimization, etc) the pulse energy was increased to $1.5\mu J$, which corresponds to a peak power of approximately $300MW$.

To further confirm that the pulse was cleanly compressed, free of an incoherent pedestal, it was focused into a 1-cm thick BaF_2 plate using an metallic mirror with an effective numerical aperture of ≈ 0.04. With $1\mu J$ pulse energy a self guided filament was formed and a supercontinuum spectrum was generated extending to the visible wavelength range.

6.4 Pulse Pair Generation

After the pulse compression was completed, one more round of spectral phase transfer measurements were done, this time with the improved FROG and full bandwidth available, as shown in Figure 6-4. This time 3 pulse pairs were generated with varying delay between the pulses (25 fs, 50 fs, and 100 fs) as might be used for in two-dimensional infrared spectroscopy. We point out that with the design of the experimental setup it is possible to impart in excess of $1ps$ of delay between the pulses, but our FROG has neither the frequency resolution nor the temporal range to characterize such a pulse pair.

6.5 Dispersion Summary

As a final verification of the simulation techniques presented in Chapter 4, the total spectral phase imparted onto the mid-IR idler by the adiabatic converter was experimentally characterized. This is possible because the net group delay dispersion of the entire OPCPA/CPDFG system is zero (it accepts a compressed pulse at the input to the stretcher and generates a compressed pulse at the exit of the compressor), so the unknown dispersion (that imparted by the adiabatic converter) can be calculated as the opposite of the sum of the rest of the dispersion in the system. This simple calculation is sufficient to characterize the group delay imparted by the adiabatic converter due to the fact that group delay adds linearly in a linear optical system,
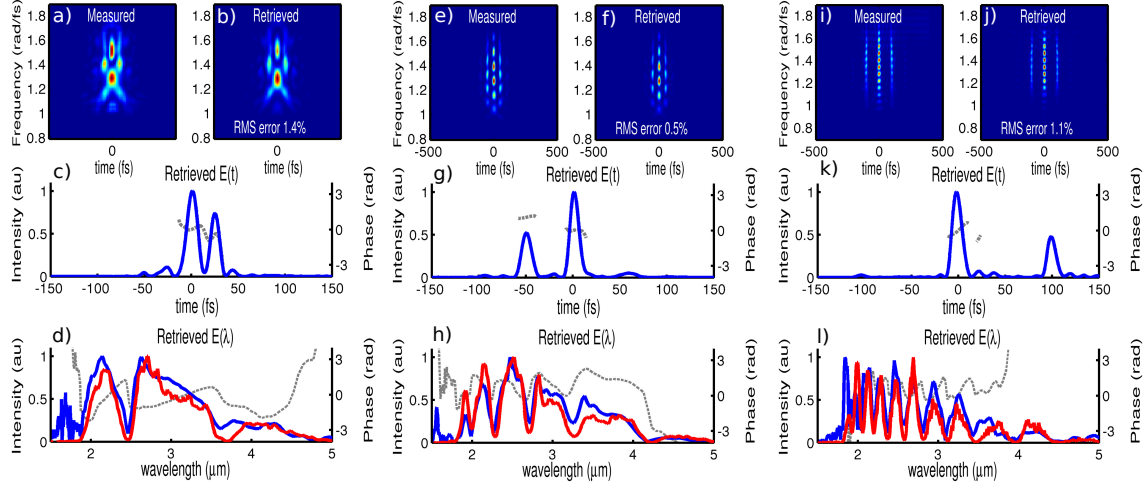
Measured and Retrieved FROG traces of pulse pairs (top row), retrieved intensity in the temporal domain (middle row; blue: intensity, gray: phase) and spectral domain (bottom row; blue: intensity, gray: phase), for 3 different input pulses. (a-d) 25 fs, (e-h) 50 fs and (i-l) 100 fs.

Figure 6-4: Generation of Single-Cycle Pulse Pairs

and all of the components in this experiment (amplifiers, pulse shapers, dazzler, etc) are chirped-pulse devices which do not impart significant nonlinear phase shifts onto the signal or idler.

The result of this calculation is shown in Figure 6-5, which shows the sum of the calculated stretcher dispersion, measured adiabatic converter dispersion, calculated adiabatic converter dispersion (as calculated using the nonlinear propagation simulation described in Chapter 4) and compressor dispersion. The residual error in the sum (which constitutes less than 1 ps of group delay in this case, consisting of approximately $750 fs^2$ of GDD and $-4500 fs^3$ of TOD) indicates the total error between the simulations and experiments (including any possible errors in the adiabatic conversion group delay, and stretcher/compressor/dazzler group delays) so it is likely that a large portion of this residual error is due to other experimental errors. In particular, different references for the dispersion of silicon at these wavelengths give significantly different values for compressor dispersion. For this study the classic values reported by Salzberg and Villa were used.

In any case, these measurements provide unambiguous proof that not only is the spectral phase of the near-IR transferred to the mid-IR, but that the additional phase
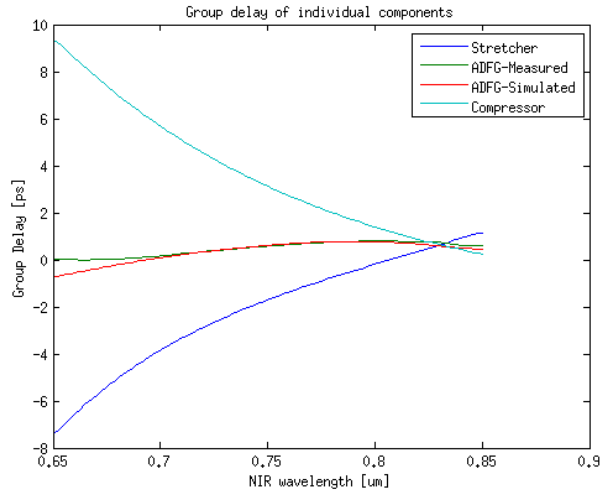
Figure 6-5: Dispersion Summary

can be, to within experimental error, modeled by the simulations presented in Chapter 4. Furthermore, it was experimentally verified that changes in both the pump and signal intensity do not measurably change the compression of the pulse when varied over 1 order of magnitude (pump intensity varied from $12GW/cm^2$ to $1GW/cm^2$ and signal energy varied from $1.5\mu J$ to $0.15\mu J$), which offers additional confirmation that the adiabatic transfer is behaving as expected.

Chapter 7

Amplification of the mid-IR Pulses in CSP and ZGP

While the concept of CPDFG and ADFG can be used to generate idler pulses extending down into the THz (in fact, as constructed the optical system used for this demonstration is capable of generating difference frequencies down to arbitrarily low frequencies, because the bandwidth of the seed source includes the ADFG pump wavelength), the $LiNbO_3$ nonlinear medium used for this demonstration is only transparent to approximately $4.5\mu m$ so it cannot be used to generate wavelengths in the $5 - 10\mu m$ wavelength range. This issue could be solved by using a different material for the nonlinear grating which is transparent at these wavelengths, however there are currently no commercially available materials which are transparent beyond $5\mu m$ and can be periodically polled for seeding/pumping in the near-IR. Furthermore, it is hard to increase the energy of the generated pulses using this technique to greater than few-microjoule energies due to practical limitations in the manufacturing process of the nonlinear gratings which prevent crystal apertures larger than a few millimeters from being produced. A solution which solves both of these issues is to use traditional OPA or OPCPA techniques to amplify the generated signal, and generate an idler which spans further into the mid-IR.

As it turns out, there is a wide variety of nonlinear optical materials which, when pumped at roughly $2 - 3\mu m$, offer incredibly large phase matching bandwidths[34]
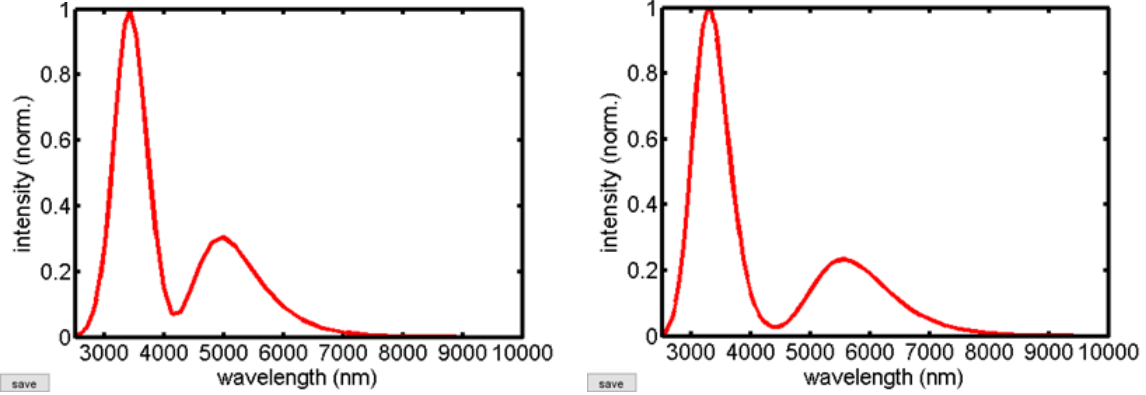
Simulated spectrum of signal and idler generated in a $1.1mm$ thick CSP crystal (left) and $0.5mm$ thick ZGP crystal (right) with $250GW/cm^2$ pump intensity

Figure 7-1: Simulated Gain Spectrum in OPA

(even supporting octave spanning spectra) and very high nonlinear coefficients (approaching $100pm/v$, 2 orders of magnitude higher than BBO). Given the availability of a high power femtosecond pump laser operating at $2.1\mu m$ (described at length in Chapter 8), two optical materials were selected for further analysis–Zinc Germanium Phosphide (ZGP) and Cadmium Silicon Phosphide (CSP)[34] . At the time the experiments were carried out it was not possible to purchase CSP commercially, however a samples of both CSP ($1.1mm$ thick) and ZGP ($0.5mm$ thick) were provided by P. Schunemann at BAE systems to support this study.

Before beginning experiments, detailed simulations were performed for both of the proposed crystals, using the simulation suite written by T. Liang, et al, which is described in detail in Reference [38]. These simulations use a split step 3-D (2 space and 1 time dimension) simulation, which takes into account all of the possible second order TWM mixing processes in addition to higher order effects such a self focusing and superflourescense, which allows it to produce accurate simulations results even when the complex interplay between pump depletion, self focusing, varying transverse profile of the various beams, etc have significant impacts on the generated beam. The frequency domain results of these simulations are shown in Figure 7-1, and the time domain results of this simulation are shown in Figure 7-2.

As can be seen from the frequency domain results, the gain bandwidth of both of the crystals are nearly identical and both crystals are capable of producing idlers
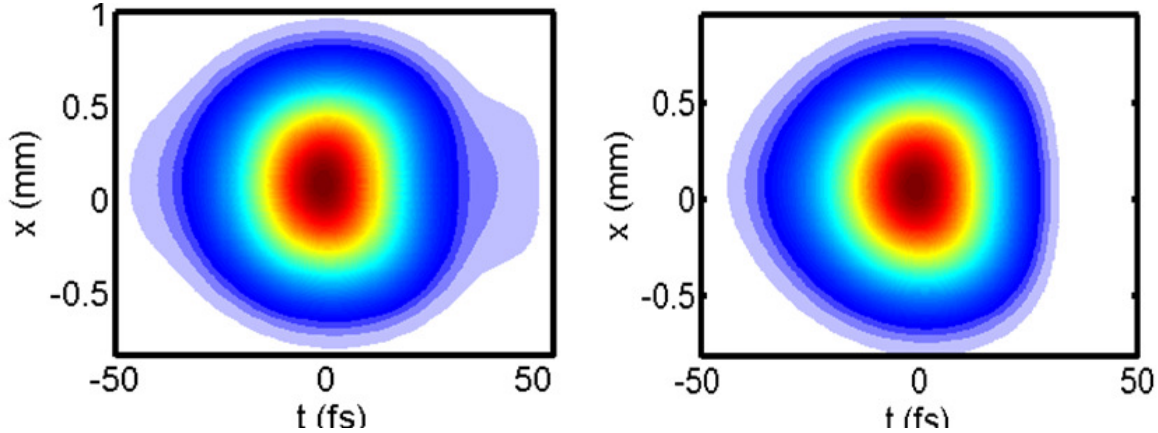
Simulated spatiotemporal profile of the idler generated in a $1.1mm$ thick CSP (left) and $0.5mm$ thick ZGP crystal pumped with a $30fs$ $2.1\mu m$ pump pulse with $250GW/cm^2$ pump intensity. The generated idler is close to diffraction limited in the transverse dimension and within 3% of its Fourier transform limited duration temporally in both cases.

Figure 7-2: Simulated Spatiotemporal Profile in OPA

which cover the nearly octave spanning bandwidth of $4.5 - 7\mu m$, which is expected because the crystals have very similar phase matching conditions (despite the fact that ZGP is negative uniaxial, as is BBO, while CSP is positive uniaxial). Furthermore, as can be seen from the time domain results shown in Figure 7-2, the idler produced from both of these crystals has a clean Gaussian spatial profile free of spatial chirp, and even nearly free of spectral chirp, being within 3% of its Fourier limited duration for both crystals. These properties make both CSP and ZGP very promising candidates to be used as OPAs seeded by the $2.6\mu m$ pulses generated by the ADFG-based source to generate intense ultra-broadband pulses in the mid-IR.

Given the promising simulation results, an OPA was constructed to evaluate these two nonlinear materials. The pump source was an OPCPA based laser, described in Chapter 8, providing $2.1\mu m$ pulses with $30fs$ duration and up to $3.5mJ$ energy (only $1mJ$ of which was used, due to the limited crystal apertures available). The seed was provided by the ADFG-based source described in Chapter 6, with the bandwidth intentionally narrowed to generate a pulse with roughly $30fs$ duration centered at $3.5\mu m$, as shown in Figure 7-3, with approximately $100nJ$ pulse energy incident on the OPA.
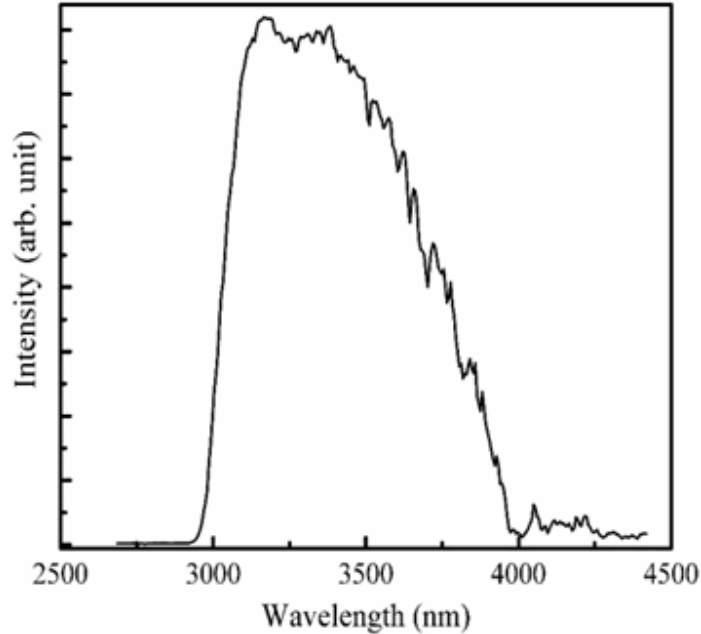
Figure 7-3: Spectrum of seed source for OPA

Due to the limited availability of ultra-broadband dichroic mirrors (in particular dichroic mirrors which have well behaved dispersive characteristics, as needed for use in ultrafast laser systems) simple uncoated silicon plates oriented at Brewster's angle were used to combine the pump/signal and separate the pump from the signal/idler. The OPAs both used Type I phase matching, so the pump was orthogonally polarized to the signal/idler, so a silicon Brewster plate oriented to pass the pump beam provides approximately 80% reflection of the orthogonally polarized signal/idler, and because the signal/idler are always in reflection it does not impart significant chirp onto them. The first experiments performed on the new amplifier were a simple output energy comparison of the CSP and ZGP based OPAs. The pump intensity was increased up to $1mJ$ (roughly $250GW/cm^2$ incident on the OPA), and the idler energy was measured after a $4.5\mu m$ long-pass filter, as shown in Figure 7-4. Even at these high pump intensities no damage was observed on either the CSP or ZGP crystal, which shows that the thin crystal thicknesses used for this demonstration can safely be used with femtosecond $2\mu m$ pump lasers. With CSP it was possible to get up to $7\mu J$ pulse energy and with ZGP it was possible to get $4\mu J$ pulse energy in the idler. These value are quite low, however this is largely due to the significant losses
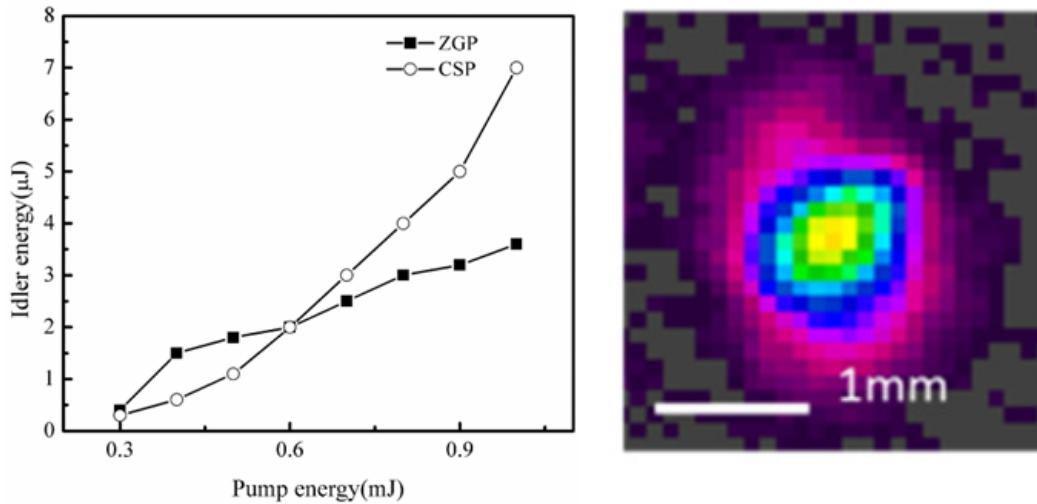
Left: Plot of idler energy vs pump energy for both ZGP and CSP based OPAs. Right: Idler Beam profile measured from ZGP OPA

Figure 7-4: Idler Energy vs Pump Energy in OPA

in the system (the uncoated crystal surfaces introduce a $\approx 50\%$ reflection, each of the beam splitters introduce a $\approx 20\%$ loss on reflection, etc) and the relatively high gain of the amplifier (in excess of 100 when the spectral overlap of the signal and idler are considered). Furthermore, when the large quantum defect (pumping at $2\mu m$ and generating at $6\mu m$) is considered, the photon conversion efficiency within the amplifier itself is on the order of 5%. The beam profile was also measured using a pyroelectric camera (Spiricon Pyrocam), as shown in Figure 7-4, and is a nearly-Gaussian beam as expected. Clearly there are significant gains to be had in terms of output power, however the focus of this study was the spectral and temporal properties of the generated pulses and not so much the output energy as even a few microjoules are sufficient for many experiments such as filamentation studies and nonlinear spectroscopy.

After confirming the output power from the parametric amplifiers, the spectra of the signal and idler were measured using a scanning grating monochromator (Horiba MicroHR), and are shown in Figure 7-5. The measured idler spectrum was actually slightly broader than predicted, spanning $4.5 - 8.5\mu m$ in CSP and $4.5 - 9\mu m$ in ZGP, despite the fact that these crystals start to become absorbing beyond $6\mu m$ and $8\mu m$ respectively. However, due to the thin crystal thicknesses used in this
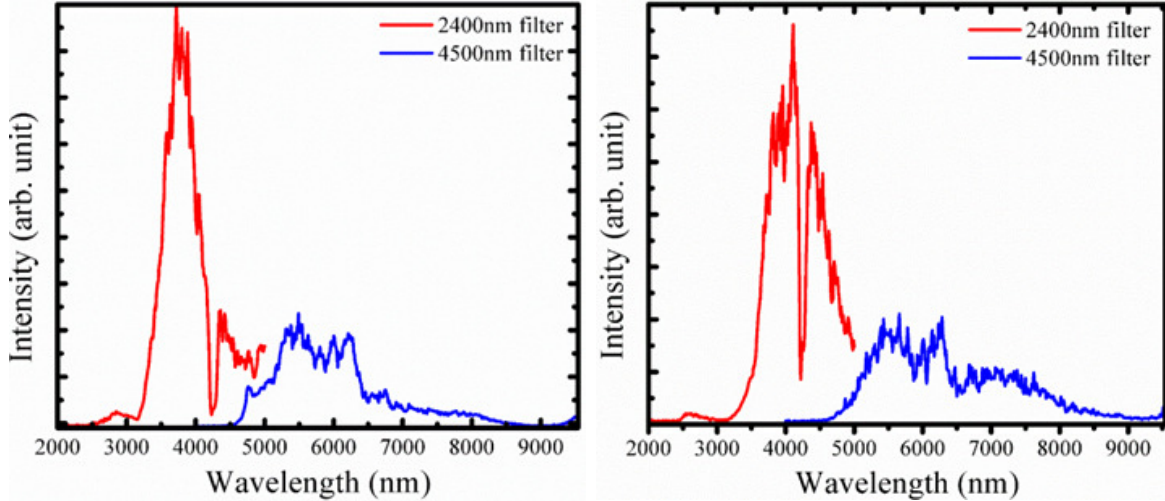
Measured idler (blue) and signal (red) spectra generated in a 1.1mm thick CSP crystal (left) and 0.5mm thick ZGP crystal (right). The dip at 4.2μm is due to atmospheric CO_2 absorption

Figure 7-5: Measured Signal and Idler Spectrum

demonstration the absorption within the crystals was only a few percent over the generated wavelength region.

Finally, the pulse duration of the generated idler was characterized in a home-built second-order balanced interferometric autocorrelator, a schematic of which is shown in Figure 7-6. Due to the limited availability of ultra-broadband beam splitters (in particular those with well behaved chirp as needed for this application), a simple Fresnel reflection from a ZnSe plate was used. ZnSe was selected because it has a relatively high index of refraction (2.5), so the Fresnel reflection at the 45° incident angle is nearly 20%, and because it has anomalous dispersion at 6μm so it can be used to partially compensate for the normal chirp introduced by other optics in the optical system. A 30μm thick GaSe crystal cut at $\theta = 0^o$ and oriented at normal incidence was used as the nonlinear element, and a mid-IR polarizer was used to isolate the generated second harmonic from the fundamental signal. Furthermore, a PbSe detector (sensitive from $1.5 - 4.5\mu m$) was selected, because it is insensitive to the fundamental wavelength. Furthermore, for these experiments the 4.5μm long-pass filter constructed on a 1mm thick germanium substrate, used to isolate the idler from the signal, nearly exactly canceled the linear chirp introduced by the ZnSe beam
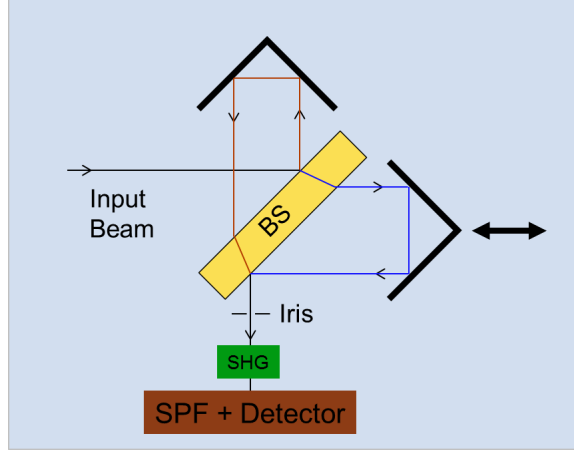
Schematic of balanced second order interferometric autocorrelator. BS - Beam Splitter (ZnSe 1 mm thick), SHG - Second Harmonic Generation (GaSe 30 um thick), SPF - Short Pass Filter (polarizer oriented to block the fundamental and pass the second harmonic), Detector - PbSe detector (Thorlabs PDA20H, sensitive from $1.5 - 4.8\mu m$)

Figure 7-6: Autocorrelator Schematic

splitter. However, the TOD of both of these materials is positive, so they add, and as a result there is approximately $5000fs^3$ of residual chirp on the pulses, which adds some temporal wings to the compressed pulse, which are visible in the autocorrelations.

Due to its higher efficiency, CSP was evaluated first, and the measured auto-correlation of the idler generated is shown in Figure 7-7, along with a simulated autocorrelation trace generated assuming a perfectly compressed pulse. From this autocorrelation it is clear that there is some spectral phase left on the pulses, which is largely attributed to the residual TOD and some uncompensated linear GDD. The Fourier transform limited duration of the generated idler pulse is $33fs$ (1.8 optical cycles at the central wavelength of $6\mu m$).

The situation with ZGP however is greatly improved, as can be seen in the auto-correlation shown in Figure 7-8. In this case the pulse shows some temporal wings, as expected given the residual TOD chirp in the system, however the FWHM duration of the pulse appears to be be nearly compressed to its Fourier limited duration of $33fs$ (1.8 optical cycles at the central wavelength of $6\mu m$). Furthermore, it was found that if the idler was focused into a $5mm$ thick BaF_2 plate it was possible to generate an intense supercontinuum spanning into visible range, which confirms that the pulse is
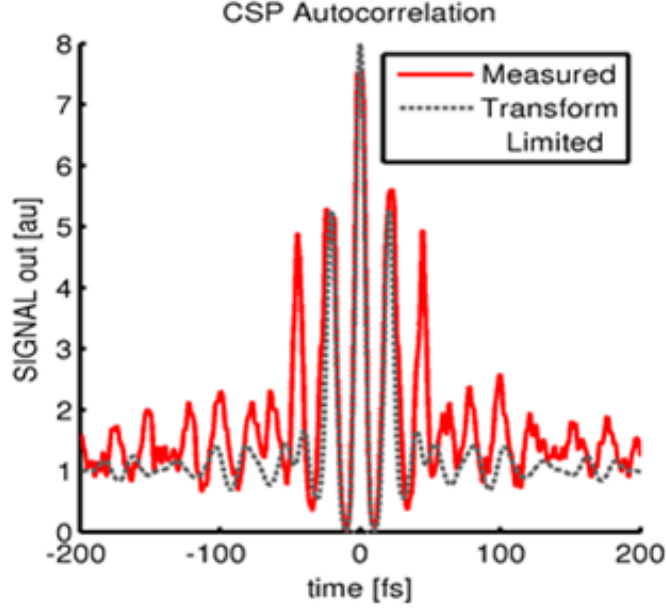
Measured autocorrelation of the idler generated in CSP, plotted against a simulated autocorrelation calculated assuming a transform limited pulse duration, which is $33fs$ (1.8 optical cycles at its central wavelength of $6\mu m$)

Figure 7-7: Measured Autocorrelation in CSP

in fact a highly intense, compressed pulse.

These results show that both CSP and ZGP are viable materials for generating ultra-broadband pulses in the mid-IR, and that when using a femtosecond pump laser at $2\mu m$ it is possible to use very thin crystals (as thin as $0.5mm$) which have extremely broad phase matching and impart minimal chirp on the generated pulses. These results contrast those previously reported by groups using picosecond pumping[58][56], as needed to take advantage of the high pump energies provided by Ho:YLF laser systems. By using a femtosecond pump laser, it is possible to use much higher intensities in the OPA, which allows the use of thinner crystals which allow for broader phase matching and correspondingly shorter amplified pulse durations. This comes at the cost of requiring a femtosecond pump laser and large crystal aperture, as is necessitated by the high peak intensities associated with a femtosecond pump laser. One interesting hybrid solution to take advantage of the ultra-broadband phase matching provided by femtosecond pumping and the high energies achievable with Ho:YLF laser systems is to use an intermediate nonlinear compression stage, for example by
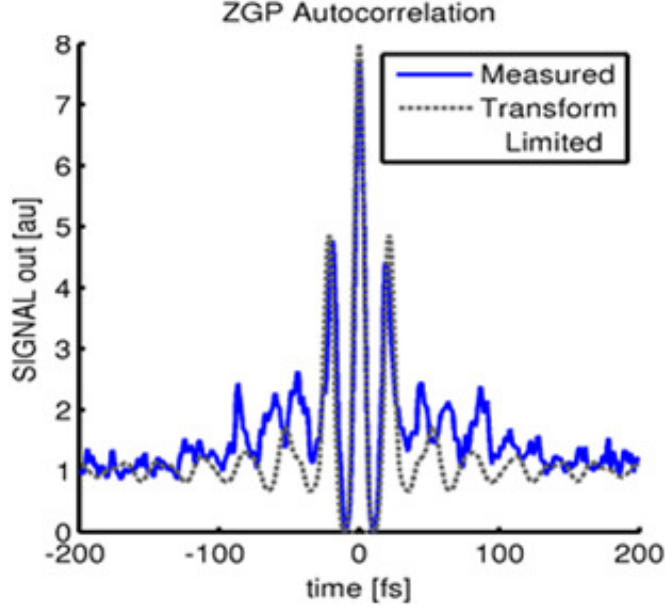
ZGP Autocorrelation

Measured autocorrelation of the idler generated in ZGP, plotted against a simulated autocorrelation calculated assuming a transform limited pulse duration, which is $33fs$ (1.8 optical cycles at its central wavelength of $6\mu m$)

Figure 7-8: Measured Autocorrelation in CSP

spectrally broadening the pulse using a gas filled capillary[15] or dielectric[42] to compress the pulse to femtosecond duration, then use an OPA to take advantage of the ultra-broadband bandwidths achievable with femtosecond pumping. Furthermore, the inherent gain narrowing in a OPA (due to the exponential dependence of gain on pump intensity) enhances the relatively poor pulse contrast possible with nonlinear compression, so the pulse will naturally be 'cleaned up' by the OPA. Furthermore, it may make sense to use a hybrid approach where a small amount of chirp is present in the amplifier, which offers the benefits of OPCPA (better energy scaling due to the lower peak intensity in the amplifier and more flexible dispersion management) with the benefits of femtosecond pumping in CSP and ZGP (extremely broad bandwidth). This approach is also quite conveniently combined with CPDFG/ADFG, whereby a shaped near-IR laser system is converted to $\approx 3\mu m$, and then the *chirped* output from the adiabatic converter is used to seed the mid-IR pumped OPCPA system, to generate another chirped idler with spectral phase controlled by the pulse shaper operating in the near-IR. This idler can then easily be compressed in a mid-IR bulk

material by using the spectral phase transfer made possible through CPDFG, which eliminates the need for complicated/lossy grating/prism compressors operating in the mid-IR.

Chapter 8

$2\mu m$ OPCPA pump laser

In addition to the mid-IR laser systems discussed in the previous chapters, significant improvements were made to the existing laser sources at MIT in an effort to make them suitable for use in the OPA demonstration discussed in Chapter 7 and to support many other experiments being carried out at MIT. These experiments include high harmonic generation[27][61], attosecond electron burst generation[65], and mid-IR filamentation studies[42][43][41][39]. A schematic diagram of the $2\mu m$ laser system is shown in Figure 8-1. These efforts were initially focused on making improvements to the $2\mu m$ laser system which was originally constructed as a part of the MIT pulse synthesizer (described in detail in [30]), but later branched out to include a complete overhaul of the OPCPA system and associated pump lasers. After careful analysis of the existing OPCPA system at MIT, it was determined that the primary source of instabilities in the system were caused by thermal variations in the lab, caused by
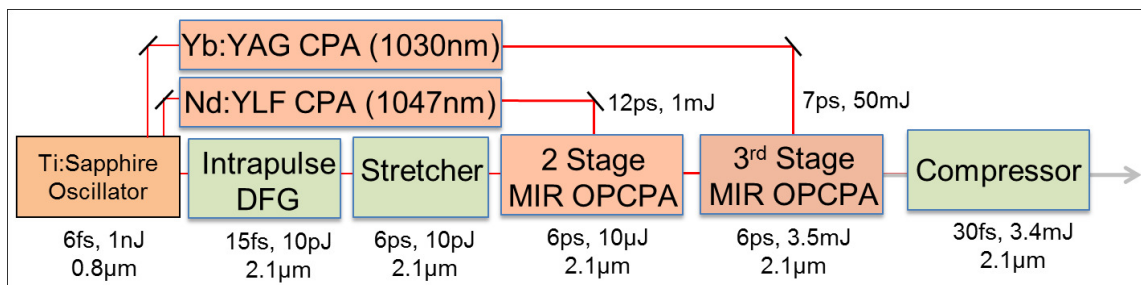

Schematic of the $2\mu m$ OPCPA system annotated with pulse durations and energies.

Figure 8-1: Schematic of the $2\mu m$ OPCPA system

equipment being turned on/off, the compressor in the air conditional system cycling on/off and even the sun rising and heating the entire building. The temperature of various points throughout the lab were logged on a 5 minute interval for 2 weeks and it was found that the temperature of the optical table varied by roughly 2^oC over the course of the day if the lab was left undisturbed (no equipment turned on, or people working in the lab) and roughly 3^oC on days when the system was in use. Based on this conclusion, it was decided that the only way to remove these drifts was to add active feedback to the laser system to compensate for the drift, as it was infeasible to correct the thermal drifts at the root of the problem. The home-built Nd:YLF CPA laser system used to pump the initial OPCPA stages was determined to be the primary cause of pointing drift in the seed system, so a beam stabilization system was added to stabilize the pointing at the output of this laser. Due to the limited availability of beam pointing stabilization systems which were capable of working with pulsed laser systems operating at low repetition rates ($1kHz$), it was decided to use a commercially available beam pointing stabilization system (Thorlabs T-Cube system based on quadrant photodiodes and piezo-electric actuated mirrors) with additional electronics added to down-convert the kilohertz signal train from the detectors to a DC signal that the controller could process. To serve this role a simple sample-and-hold circuit was build around the LM298 monolithic sample-and-hold chip, which was trigged by the master $1kHz$ trigger signal for the OPCPA system.

This system was quite successful in locking out the slow (thermally induced) drifts in the system, and reduced the drift of the pump beam on the first OPCPA stage from nearly $0.5mm$ over a 2 hour period to $0.03mm$ over the same period, as shown in Figure 8-2.

After the pointing drifts has been brought under control it was discovered that the output energy and central wavelength of the amplified beams shifted on a tens-of-minutes to hour time scale due to the relative timing of the pump pulse and the signal pulses in the OPCPA amplifier stages. These drifts were caused by slight changes in the optical path length in the regenerative amplifier used to generate the pump pulses, and can easily be attributed to slight thermal drifts of the temperature
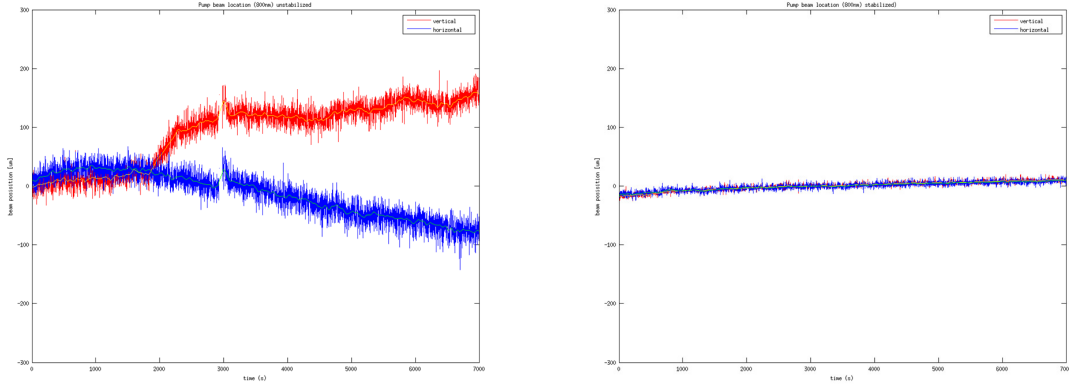
Figures showing the drift (red: vertical, blue: horizontal) of the Nd:YLF pump laser over a 2 hour period. Left - un-stabilized system, showing a drift of proximately $0.2mm$ at the first OPCPA stage point. Right- System after activating the pointing stabilization system, showing approximately $0.02mm$ drift over the same period.

Figure 8-2: Pointing Stability of the $2\mu m$ Laser System

of the regenerative amplifier (despite the fact that the baseplate of the amplifier is water cooled and regulated to within a few tenths of a degree Celsius, even these small shifts are sufficient to cause significant timing drift of the picosecond pulses over the roughly 1 nanosecond total amplification period in the regenerative amplifier due to slight changes in the round trip time). In addition to the drifts due to the regenerative amplifier, there were also slight timing drifts due to the repetition rate of the modelocked Ti:Sapphire oscillator which seeds both the pump laser and OPCPA system. This is due to the fact that a different pulse is amplified in the regenerative amplifier than is amplified in the OPCPA, in order to achieve temporal overlap of the pump and seed pulse without needing hundreds of meters of free space propagation of the seed pulse to compensate for the many round trips through the regenerative amplifier the pump pulse experiences. Both of these sources were purely thermal, and occurred over a many-minute time period, so it was possible to remove them by using a spectrometer to monitor the amplified signal spectrum (which is dependent on the pump-signal timing due to the high chirp in the OPCPA system), and moving a motorized delay line to keep the central frequency constant. This task was performed using an grating spectrometer (Ocean Optics NIR256) and a short python script which calculates the central wavelength of the measured spectrum and moves the
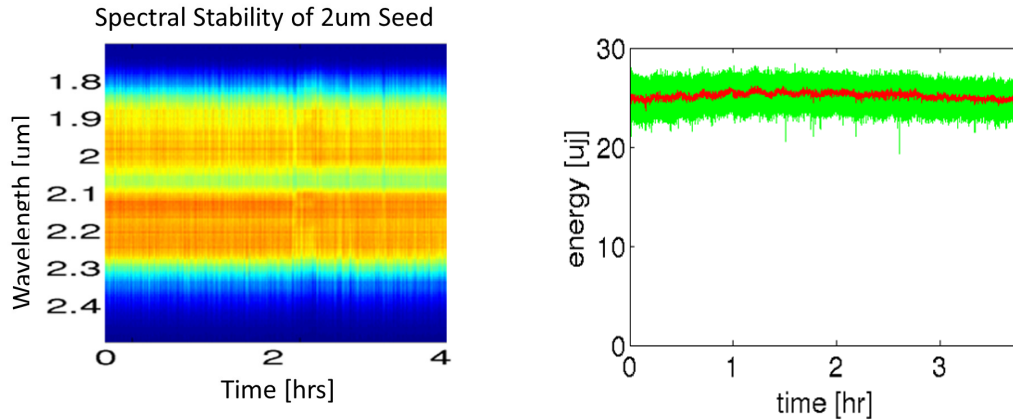
Spectral and energy stability of the $2\mu m$ seed source, with pump time and pointing locks active, measured over a 4 hour period. Energy stability is 2.5% RMS over 10 seconds and 2.8% RMS over the full measurement. Central wavelength shift is $5nm$ over the full measurement period, corresponding to a 1% shift relative to the $600nm$ bandwidth.

Figure 8-3: Spectral and Energy Stability of the $2\mu m$ Laser System

delay line based on a integrating feedback loop. After implementing this feedback system the energy, spectral, and pointing stability of the $2\mu m$ OPCPA system were sufficient for the proposed experiments. The measured performance of the $2\mu m$ laser system is shown in Figure 8-3. The energy stability was measured to be 2.5% RMS over 10 seconds and 2.8% RMS over the 4 hour measurement period, and the spectral drift was approximately $5nm$ over the measurement period, which represents a shift of 1% of the $600nm$ bandwidth.

With the renovations of the seed laser system complete it was possible to accurately evaluate the existing power amplifier stage in the $2\mu m$ OPCPA system [27], and the cryogenic pump laser system that pumps it. The evaluation and upgrades to the pump laser system are discussed at length in Chapter 9. After the pump laser upgrades were completed the amplifier performance was acceptable for the experiments proposed, and the only changes needed were tweaks to the dispersion management (to account for the shorter duration pulses produced by the upgraded pump laser system) and the addition of diagnostics to monitor the performance of the amplifier in operation. In addition to the active pointing stabilization integrated in the Yb:YAG pump laser, an active timing stabilization lock was added to remove the timing drift

between the Yb:YAG and Nd:YLF pump laser systems, using the same technique used to stabilize the seed laser system. However, due to the high cost of the mid-IR spectrometers, the seed laser system stabilization loop was switched from stabilizing the $2\mu m$ seed laser directly to stabilizing the spectrum of the first 2 stages of the $800nm$ OPCPA system used to for the ADFG work, using a near-IR spectrometer (Ocean Optics USB2000). This also stabilized the $2\mu m$ seed laser, because the $800nm$ and $2\mu m$ seed OPCPA systems are derived from the same Nd:YLF pump laser, so the timing drift from this pump laser is common to both OPCPA systems.

After these upgrades were completed the final system was evaluated and determined to be suitable for the experiments discussed in the introduction to this chapter. In this configuration the amplifier was capable of generating up to $3.5mJ$ pulse energy when pumped by the full $50mJ$ energy from the Yb:YAG pump laser. In day-to-day operation the system was run at $34mJ$ pump energy and $2.5mJ$ pulse energy, to leave a safety margin to minimize the chances of damage in the system, and leave some headroom so that day to day variations in the system performance would not affect the experiments being carried out that day. Figures 8-4 and 8-5 show measurements of the beam profile and pulse duration/spectrum after compression. The pump profile is a clean Gaussian profile, and the pulse is compressed to within 15% of its Fourier transform limited duration of $25fs$.

Finally, an active beam pointing stabilization system was added to the output of the $2\mu m$ laser system to remove any residual pointing drifts, because some experiments require coupling of the beam into a capillary or hollow core fiber and are thus very sensitive to beam pointing/centering shifts. Due to the fact that there are no readily available quadrant photodiode detectors sensitive to the $2\mu m$ wavelength range, pyroelectric quadrant detectors were used (Molectron PDQ). In order to interface these detectors with the existing pointing stabilization infrastructure (based on the Thorlabs T-Cube system) a set of custom interface electronics was assembled. This circuit which took the amplified outputs from the quadrant detector and calculated the sums and differences as needed for determining the beam position (vertical position is calculated as the difference of the sums of the top and bottom halves of
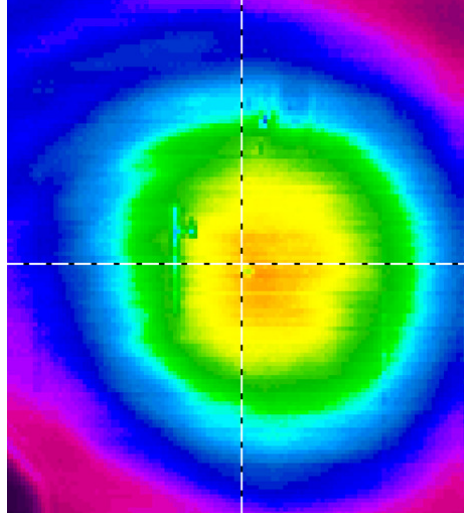
Beam profile of the amplified and compressed $2\mu m$ beam. The vertical line is a defect on the camera sensor.

Figure 8-4: Beam Profile of $2\mu m$ Laser System

the detector, and the horizontal position is calculated as the difference of the sums of the left and right halves of the detector), and then amplified and sampled these signals as required for the controller. The analog processing was done using a TL084 quad operational amplifier configured as a universal (Z = a(X-Y)) amplifier, and as with the other lasers the sample-and-hold was done using a LM298. I give thanks to Dr. Ondrej Novak who kindly prototyped this circuit during his visit to MIT.
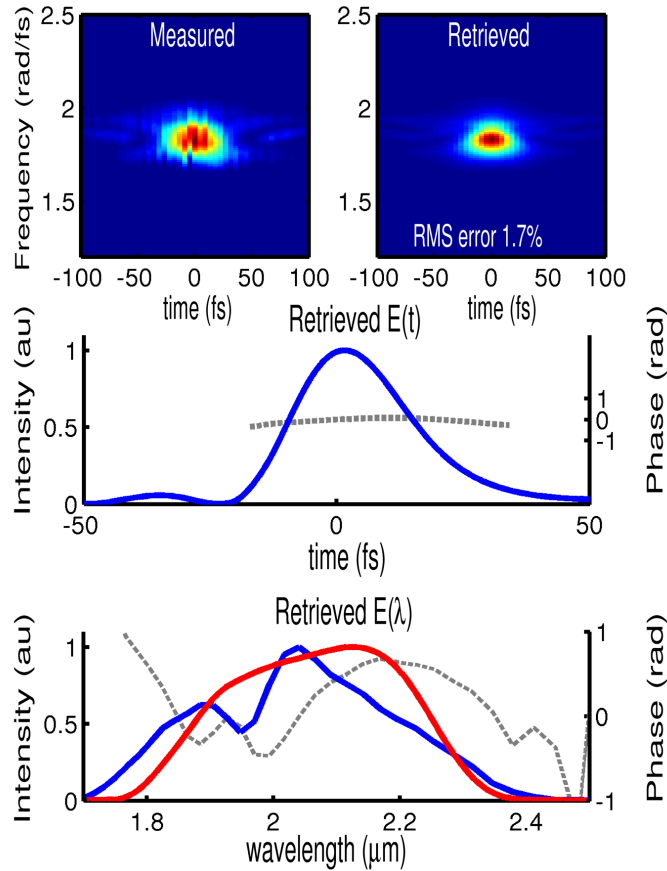
FROG measurement of the $2\mu m$ compressed pulse. Top - Measured and retrieved FROG spectrograms. Middle - Retrieved temporal intensity (blue) and temporal phase (gray). Bottom - Measured (red) and retrieved (blue) spectral intensity and spectral phase (gray). The transform limited duration of the pulse is $25 fs$, and the retrieved pulse duration is $28.7 fs$, corresponding to 4.2 optical cycles at the central wavelength of $2.05\mu m$

Figure 8-5: FROG Measurement of the $2\mu m$ laser system

THIS PAGE INTENTIONALLY LEFT BLANK

Chapter 9

1030 nm Yb:YAG Pump Laser

One of the primary advantages of OPCPA technology is that OPCPAs can be pumped by picosecond laser systems, which are capable of generating much higher powers than the femtosecond Ti:Sapphire systems commonly used for pumping OPA systems. For example, it is possible to buy a commercial $100W$ ($10kHz$ $10mJ$) Yb:YAG laser system (Amphos, Trumpf Scientific Lasers) and research systems have been demonstrated with output powers well into the kilowatts[12]. The crux of OPCPA technology is that it requires a high power pump laser with short pulse duration, because the longer the pulse duration the harder it is do the dispersion management in the OPCPA, and typically pulse durations of a few picoseconds are used for millijoule class systems. Furthermore, many of the properties of the pump laser, such as the beam profile and repeatability/stability, are transfered to the amplified beam, so it is paramount that the pump laser have, in addition to high average power, a high quality beam profile and excellent stability in order to have a high performing OPCPA system. In general it is quite hard to achieve all of the goals simultaneously, and huge amounts of research effort has gone into finding innovative ways to improve the state of the art both in fundamental advancements (such as using novel laser materials or amplification geometries) and through meticulous engineering work (such as careful optimization of the thermal management in the system or careful design of the laser to minimize alignment drifts over time).

One particularly interesting class of material for amplifying picosecond pulses

at $1\mu m$ are ytterbium doped ceramics (YAG, Vanadate, KGW, KYW, etc), which have excellent quantum efficiencies (exceeding 90% in some cases), excellent thermal properties, and sufficient gain bandwidth to support the generation of few- to sub-picosecond pulses[12][57]. For this work we elected to use ytterbium doped YAG (Yb:YAG) which is cryogenically cooled to $\approx 80K$ using liquid nitrogen. We do this because while room temperature Yb:YAG has excellent thermal properties (9% quantum defect, thermal conductivity $\approx 10Wm^{-1}K^{-1}$, thermal-optic coefficient of $8*10^{-6}K^{-1}$, and roughly $1ms$ lifetime), these values are significantly improved with cryogenic cooling (thermal conductivity increases to $\approx 39Wm^{-1}K^{-1}$, thermal-optic coefficient decreases to $9*10^{-7}K^{-1}$). This means that with cryogenic cooling the thermal lensing is the system is reduced by an order of magnitude, or equivalently it is possible to use an order of magnitude higher pump power in a given optical setup so long as one keeps the crystal at cryogenic temperatures [57].

Furthermore, the laser properties of Yb:YAG are significantly improved with cryogenic cooling. For a given pump intensity, the saturation fluence is decreased and the gain is increased, which means that it is significantly easier to extract the energy stored in the gain medium. For systems with sub- to few- nanosecond pulse durations (as is in the case with this system and most millijoule to joule class picosecond CPA laser systems), it typically requires on the order of 100 passes through the gain medium to effectively extract the energy stored in the laser crystal in a room temperature Yb:YAG system. This is easily achieved using a regenerative amplification scheme, but this results in a fairly complicated and large experimental setup, especially as the energies exceeded a few millijoules. However, with cryogenically cooled Yb:YAG it is possible to extract the same amount of energy in only a few passes, so it is possible to use a much simpler amplification geometry. For example, a saturated gain of nearly 50 was reported in a single-pass cryogenically Yb:YAG amplifier[28] consisting of 2 $23mm$ long cryogenically cooled Yb:YAG crystals with a pump intensity of roughly $10kW/cm^2$ at $940nm$ (operating in the quasi-CW regime).

The system presented here takes advantage of the unique combination of properties offered by cryogenic Yb:YAG to deliver $8ps$ pulses at $1030nm$ with pulse energies up
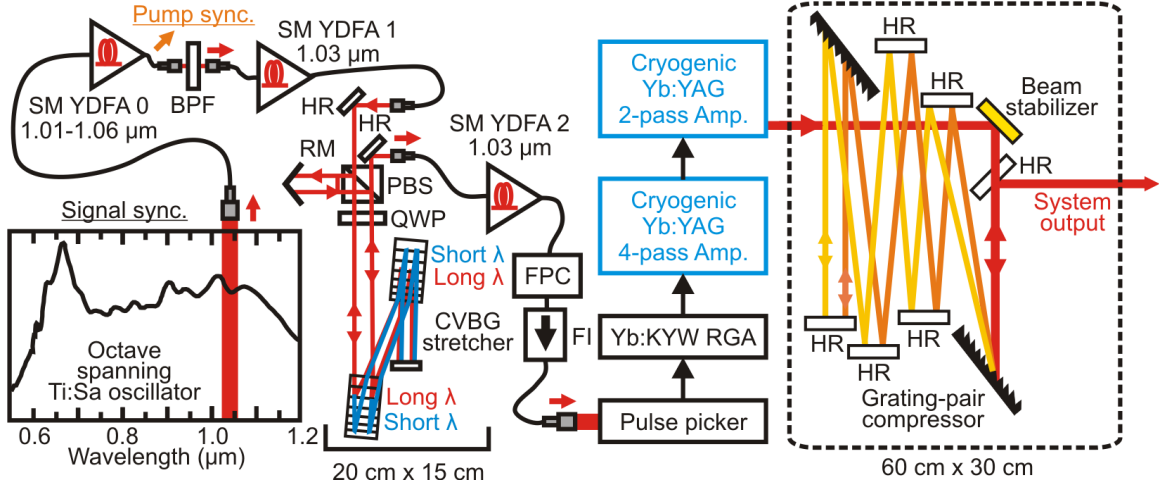
Figure 9-1: Overall schematic of the Yb:YAG Laser System. [12]

to $70mJ$ at a $1kHz$ repetition rate. Furthermore, the generated pulses have excellent beam properties, with a nearly diffraction limited beam profile having $M^2 \approx 1.1$ and free of ellipticity/astigmatism, and stability suitable for OPCPA pumping (pointing drifts of only microradians and energy drifts of only a few percent over an 8 hour operating period). This is done with a hybrid approach using a combination of Yb doped fibers, a room temperature regenerative amplifier, and pair of cryogenically cooled multipass amplifiers, as shown in Figure 9-1.

9.1   Construction

To ensure that the amplified pulses are synchronized with the rest of the OPCPA system, the Yb:YAG CPA system is seeded by the same Ti:Sapphire oscillator that seeds to the OPCPA system. A portion of the oscillator spectrum from roughly $1000-1100nm$ is picked off using a dichroic mirror, and this seed pulse is amplified in a 3-stage fiber amplifier system to roughly $1nJ$ for seeding the regenerative amplifier. This amplifier systems consists of a Yb:fiber pre-amplifier which amplified the seed pulse to roughly $100pJ$, using the full bandwidth of seed pulse, a bandpass filter to select a $\approx 4nm$ bandwidth around 1030 nm, a Yb:fiber mid-amplifier, stretcher, and Yb:fiber power amplifier to amplify the seed pulses to the $1nJ$ energy needed to overcome the amplified spontaneous emission (ASE) noise background in the regenerative amplifier.

The stretcher consists of 8 bounces off chirped volume Bragg gratings, which each provide normal dispersion of $100ps/nm$ for a total of $800ps/nm$ of chirp on the pulse, which gives a duration of $\approx 300ps$ over the $0.35nm$ gain bandwidth of the cryogenic Yb:YAG amplifiers.

The $1nJ$ pulses produced by the Yb:fiber pre-amplifier are then picked using a pulse picker based on a Pockels cell operated in single pass, $\lambda/2$ retardation mode, to generate a $1kHz$ pulse train. This is then amplified to $1.5mJ$ in a commercial regenerative amplifier (Amplitude Systems S-Pulse HP), which uses a pair of Yb:KYW gain crystals. This amplifier has a sufficiently large gain bandwidth (owing to the gain bandwidth of approximately $50nm$ available from the Yb:KYW gain medium) that despite the large gain there is virtually no gain narrowing in the amplifier. We exploit this property to keep the bandwidth of these seed pulses broader than the gain bandwidth of the multipass amplifiers, to maximize the bandwidth throughout the multipass amplifiers. This has the added advantage that, for a given chirp rate, this maximizes the chirped pulse duration in the amplifier, and thus minimizes the chirped pulse intensity. Of course this also reduces the compressed pulse duration, however this was not of particular importance in this system because the downstream OPCPA system can be optimized for pulse durations from $5-20ps$ by simply adding or removing dispersive elements.

The cryogenic amplifier then amplifies the $1.5mJ$, chirped, $1030nm$ pulses from the seed system, and produces up to $70mJ$ pulse energy before compression. There are of course many constraints placed on the design of this amplifier, ranging from practical issues such as the availability of specific pump lasers and gain crystals for use on the project to physical limitations such as intensity constraints to avoid optical damage or the accumulation of nonlinear phase (B-integral) throughout the system. The gain crystals, cryogenic dewars, and pump lasers were all purchased as semi-custom parts, and had previously been used in the amplifiers described in References [28] and [26] (as were the stretcher and compressor). The crystal used were 1at% and 2at% doped (for the 1st and 2nd stage respectively) Yb:YAG, which were indium soldered to a sapphire heat-spreader. This was then in turn bolted to a copper

cold-plate, which is immersed in liquid nitrogen, which keeps it at roughly $80K$. At the heat loads used for this project ($100 - 200W$ pump powers, and a few tens of watts dissipated by the crystal) simple evaporative cooling of atmospheric pressure liquid nitrogen is sufficient, however the cold plates have pins machined into them to maximize the contact area with the liquid nitrogen to eliminate the possibility of flash boiling causes issues due to the the Leidenfrost effect. The diode pump modules are commercially available (Laserline LDM) fiber coupled laser diodes, which use highly multimode fibers ($0.6mm$ diameter) to deliver the laser radiation to the experimental setup.

These systems also provided valuable insight on where the trouble issues in the existing laser system were, and baseline performance data which was invaluable when designing the improved amplifier system. The primary change made in the work presented here was the replacement of the home-built cryogenically cooled Yb:KYW regenerative amplifier with the commercially produced room temperature regenerative amplifier, which provided significantly better stability and much broader bandwidth. This regenerative amplifier also produced much less energy (roughly $1.5mJ$ available for use in the multipass amplifier) than the previous amplifier (which produced roughly $10mJ$), so the gain in the multipass amplifier needed to be increased to compensate for this lower seed energy. Furthermore, because the bandwidth produced by the new seed system ($\approx 1.5nm$) was broader than the gain bandwidth of the multipass amplifier ($\approx 0.35nm$), a design choice made to maximize the bandwidth in the amplifier, the actual effective energy available to seed the amplifier was less than $1mJ$. To recover this order of magnitude drop in seed intensity the first multipass amplifier was rebuilt in a 4-pass configuration (increased from 2 passes previously), as shown in Figure 9-2.

In order to achieve 4 passes through the crystal, without introducing any astigmatism or ellipticity into the beam, a collinear geometry was constructed using a double-folded geometry. The first 2-passes are separated using a combination of quarter wave plate and polarizer, and the 3rd and 4th passes are separated using a Faraday isolator arranged to act as a circulator. This allows for the pulse to pass 4
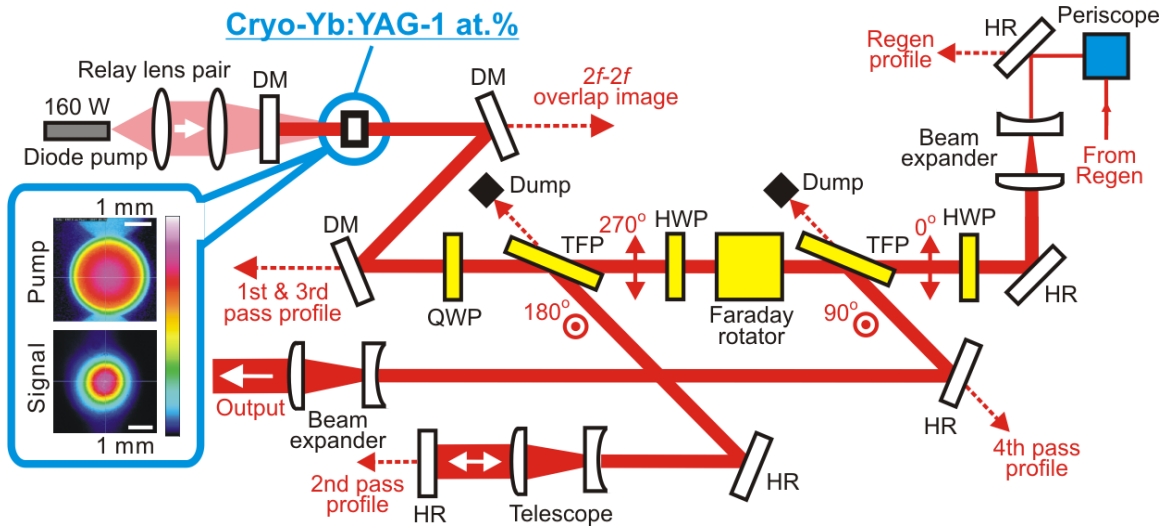
Detail schematic of 1st cryogenic multi-pass amplifier. HR - High Reflector. HWP - Half Wave Plate. TFP - Thin Film Polarizer. QWP - Quarter Wave Plate. DM - Dichroic mirror (reflect 1030 nm, transmit 940nm). Inset - Pump and Amplified beams imaged at the center of the Yb:YAG crystal. [12]

Figure 9-2: Detail Schematic of 1st MPS Amplifier

times through the crystal, with each pass exactly collinear to the pumped region in the crystal, which allows the generation of an excellent quality beam ($M^2 = 1.06$) with no measurable astigmatism or ellipticity. Furthermore, by expanding the seed beam to be larger than the pumped region in the crystal this amplifier acts as a soft aperture which spatially filters out the slight ellipticity present in the seed beam without introducing any hot-spots or diffraction rings on the beam.

Furthermore, due to excellent thermal properties of Yb:YAG the thermal lens introduced in the crystal has a focal length of roughly $1m$ at the $150W$ pump power used for this work, which can easily be compensated by placing a negative lens or concave mirror on the system. Conveniently, this configuration places a retro-reflection between the 2nd and 3rd passes in the amplifier, which provides a location to place a compensating element to compensate for the thermal lens introduced in the Yb:YAG crystal. To add an additional degree of freedom into the thermal lens compensation system (as is useful to allow quickly re-optimizing the system for varying pump intensities), an 'adjustable curvature mirror' was used, consisting of a flat mirror and a pair of lenses arranged as a simple Galilean telescope. The magnification of the telescope

88

is not important (because the beam passes through it twice it only affects the size of the beam on the flat mirror), however if it is de-focused by moving the central lens, the net effect is that the reflected beam has a wavefront as if it has been reflected from a curved mirror with radius of curvature related to the detuning of the lens position. In this fashion the thermal lens from the first 2 passes through the crystal can be compensated for, and the thermal lens from the 3rd and 4th passes can be pre-compensated for. Finally, the output beam (after all 4 passes) is passed through another telescope to increase the beam size before it enters the main amplifier, and this telescope can be fine tuned to to remove the residual thermal lens after the 3rd and 4th passes of amplification. Note - in general using telescope in an unfocused configuration like this can cause problems with the wavefront of the beam (especially in systems with flattop beams), however in this system care is taken to ensure that the beam remains Gaussian throughout the system, so this is not an issue.

When designing amplifiers it is always important to consider the intensity of the beam throughout the system, and when working with short pulses one must also consider the nonlinear phase accumulated in the system. In this amplifier the amplified beam in the crystal is slightly under $2mm$ in diameter (measured at $1/e^2$), and the energy is no more than $30mJ$, so the fluence is on the order of $1J/cm^2$ which is on the high side for the $\approx 200ps$ pulse duration used in the system, but so long as high quality optics are used is acceptable. However, while the B-integral in the Yb:YAG crystal is negligible, the Faraday rotator has an unfortunate combination of long crystal length (tens of millimeters) and high nonlinear index n_2 (approximately 8 for the TGG ferro-optic crystal), so with the intensity used in this system there is significant B-integral accumulated in the rotator, which is in excess of a radian when operating at the full output power of $30mJ$. This manifests itself as self focusing of the beam, with an effective lens introduced in the Faraday isolator on the amplified beam as it exits the amplifier. The focal length of this effective lens was measured to be several meters, so it can be managed by slightly de-tuning the output telescope to maintain the correct beam size of the amplified beam as it enters the second amplifier stage. This issue could be avoided by placing a telescope between the Faraday rotator and

Detail schematic of 2nd cryogenic multi-pass amplifier. HR - High Reflector. HWP - Half Wave Plate. TFP - Thin Film Polarizer. QWP - Quarter Wave Plate. DM - Dichroic mirror (reflect 1030 nm, transmit 940nm). ML - Meniscus Lens. Inset - Pump and Amplified beams imaged at the center of the Yb:YAG crystal. [12]

Figure 9-3: Detail Schematic of 2nd MPS Amplifier

the Yb:YAG crystal to increase the beam diameter in the Faraday rotator, however due to space constraints it was not practical to add one.

With a pump energy of $100W$ (absorbed into the Yb:YAG crystal), it was possible to get $30mJ$ energy out of this amplifier with $1.5mJ$ energy from the seed system. This efficiency is relatively poor (30% compared to the theoretical 91% considering only the quantum defect), which is largely due to the fact that the system is only being run at $1kHz$ and the lifetime of cryogenically cooled Yb:YAG is only $0.85ms$, so a significant amount of the pump energy is lost to ASE in the crystal. Furthermore, a Gaussian amplified beam is used, which does not have perfect overlap with the top-hat pump profile (shown in the inset of Figure 9-2), so there are some overlap losses.

The resulting $30mJ$ beam produced by the first amplifier stage is further amplified using a 2-pass second stage amplifier, which also consists of a cryogenically cooled Yb:YAG gain medium. As shown in Figure 9-3, this amplifier is configured in a simple collinear 2-pass geometry using a quarter-wave plate and polarizer to separate the 2 passes. Furthermore, as in the first amplifier, the thermal lens in this amplifier is also
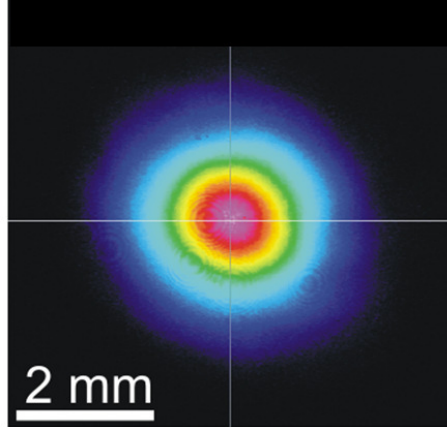
Figure 9-4: Measured beam profile of the amplified beam. [12]

roughly $1m$, so a negative lens with $1m$ focal length is inserted before the Yb:YAG crystal, which serves to roughly compensate the thermal lens. The input and output telescopes can then be used to fine tune the collimation in the system and beam sizes in the amplifier. To minimize the slight astigmatism introduced by the one-sided cooling of the Yb:YAG crystals a 90° rotating periscope was used to rotate the beam between the 1st and 2nd amplifiers.

This amplifier is pumped with up to $150W$ (absorbed) pump power, and in this configuration it was possible to achieve output energies up to $70mJ$. To ensure that there is sufficient headroom to absorb fluctuations in output power (due to slight misalignments, variations in seed performance, etc) and to provide a safety margin between the beam intensity and the damage threshold of the optical components, the system is run at $50mJ$ for normal operation. The measured beam profile at the exit of the amplifier is shown in Figure 9-4, which shows that the beam has a clean Gaussian profile, and the M^2 of the bean was measured to be 1.15.

After the second stage amplifier the amplified pulses are compressed in a grating compressor. To maximize the compression efficiency, high performance dielectric gratings (fabricated at Lawrence Livermore Laboratories) with a groove density of $1700lines/mm$ were used in a nearly-Littrow configuration, and provide approximately 97% diffraction efficiency. The spacing between the gratings was experimentally optimized to minimize the duration of the compressed pulses at 4.2 meters from
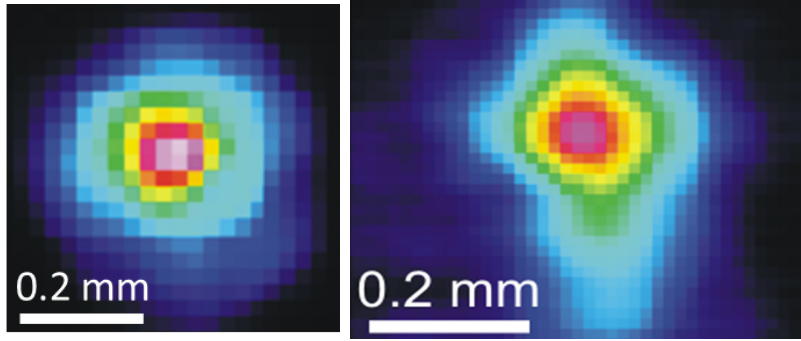
Left: Beam profile of green beam (at focus). Right: Beam profile of DUV beam (at focus). [12]

Figure 9-5: Beam Profile of Second and Fourth Harmonic

grating to grating, and in this configuration pulses of approximately $6ps$ FWHM duration were produced. With careful optimization of the grating angles it was possible to preserve the nearly diffraction limited beam profile produced from the multipass amplifier system on the compressed beam.

Additionally, the generated beam was converted to green (515 nm) and the deep ultraviolet (DUV, $257nm$) using cascaded second harmonic generation first in LBO and then in BBO. The wavelengths are needed for OPAs operating in the near-IR and visible respectively, to satisfy the energy conservation requirement that the pump have a higher photon energy than the signal. The LBO used was a $15mm$ thick $12mm$ aperture LBO crystal, which was cut for noncritical temperature-tuned phase matching ($\theta = 90$, $phi = 0$, crystal temperature $= 190$ C). In this configuration it was possible to generate up to $12mJ$ of green using up to $30mJ$ of pump energy, limited by the crystal aperture[25]. Furthermore, this was then frequency doubled again to $257nm$ in a $0.5mm$ thick BBO crystal cut for type I second harmonic generation ($\theta = 48$, $phi = 90$) to produce up to $2.2mJ$ in the DUV. Both of these beams had a top-hat ($M^2 < 3$) profile after conversion, due to saturation effects, however they could both be focused down to roughly Gaussian spots, as shown in Figure 9-5.
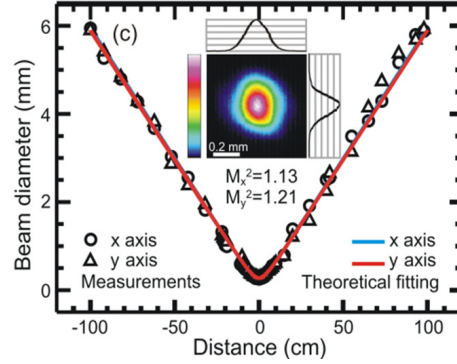
M^2 measurement of the amplified beam, showing fit to a Gaussian beam. Inset - Focused beam profile. [12]

Figure 9-6: M^2 Measurement of Amplified Beam

9.2 Performance Verification

As with any ultrafast laser system, extensive performance verification must be carried out before putting a system into use, because there is a large number of possible issues which can be present that go unnoticed until the laser is used for ultrafast work, such as improper compression, the presence of pre/post pulses, the presence of spatial chirp, timing jitter, etc.

The first verification done on this system was an evaluation of the spatial properties of the pulse. The M^2 was measured by focusing the beam using a $1m$ focal length lens and comparing the spot size through the focus to a diffraction limited Gaussian beam, and calculated to be 1.13 in the X-axis and 1.21 in the Y-axis, as shown in Figure 9-6. The slight asymmetry is due to the one-sided cooling of the Yb:YAG crystal, which causes a thermal one-direction thermal gradient in the crystal, which in turns introduces a slight asymmetry in the beam properties in the horizontal and vertical axis.

Next, the temporal properties of the pulse were characterized. The pulse duration was measured using an autocorrelator (APE PulseCheck), and the spacing between the gratings in the compressor were adjusted to minimize the pulse duration. In this fashion it was possible to compress the pulse to roughly $6ps$, however for final operation the pulse was chirped slightly (by detuning the spacing between the gratings in the compressor) to give an $8ps$ pulse duration, as shown in Figure 9-7.
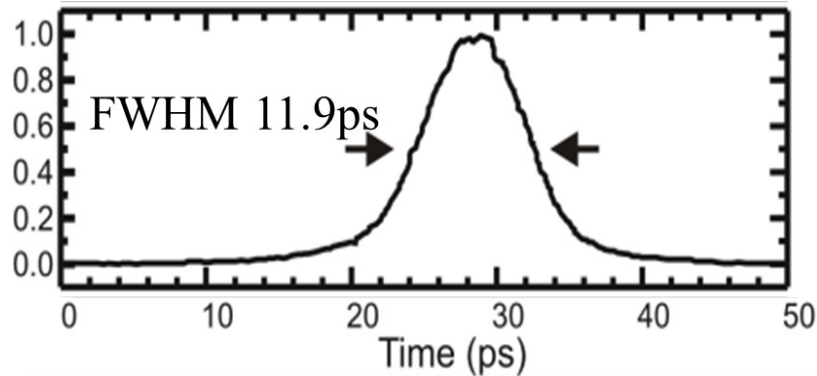
Autocorrelation of compressed beam. Deconvolved pulse duration (FHWM) is 8.4*ps*. [12]

Figure 9-7: Autocorrelation of Compressed Beam

The longterm stability of this system is of critical importance for it to be a useful research tool, so significant effort was put into evaluating and minimizing drifts in the system. Thermal variations were minimized by adding water cooling to all of the heat producing elements on the optical table (including the the vacuum chamber in which the Yb:YAG crystals are mounted, the beam dumps that collect the pump light which is not absorbed into the Yb:YAG crystal, and the beam dumps that the unused amplified beams are dumped into) and ensuring that the lab remained at a constant temperature. However, due to very long path lengths in the system (roughly $5m$ total path length) it was not practical to reduce the thermal drifts to acceptable levels. Instead, an active beam pointing system was added, using the same technique used to stabilize the Nd:YLF laser discussed in chapter 8. Careful effort was taken to image the position sensitive detector used to lock the beam position exactly to the crystal face of the OPCPA amplifier in use, so that the beam centering was exactly locked in the desired position, with a minimum amount of drift introduced to residual pointing errors. This reduced the long term drifts to microradian levels, or as measured at the OPCPA amplifier in the $2\mu m$ laser system centering shifts of less than 1% of the beam diameter. The beam pointing was measured over an 8 hour workday using a CCD camera (Dataray WinCamD) at 1 measurement per second, using a $1ms$ integrating time so that the shot-by-shot beam position was recorded. The results of this test are shown in Figure 8-3, which shows negligible drift and a

94
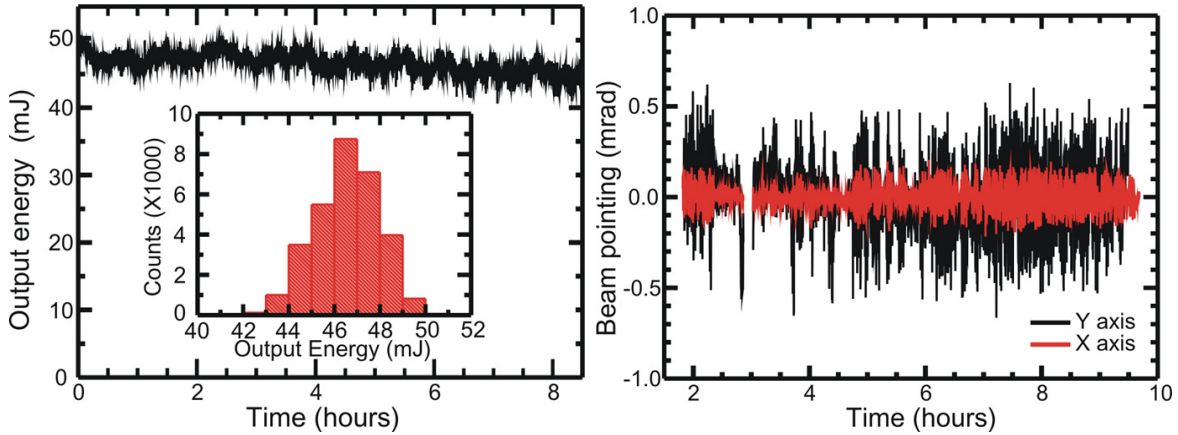
Energy and pointing stability of amplified beam, over an 8 hour period. Left: Energy stability Inset: Pulse energy distribution. Energy stability is 1% RMS over 10 seconds and 3.5% RMS over the full 8 hour measurement period Right: Pointing stability. Pointing stability is $6\mu Rad$ RMS in the vertical and $2\mu Rad$ RMS in the horizontal. [12]

Figure 9-8: Energy and Pointing Stability of Amplified Beam

RMS beam pointing fluctuation of $6\mu Rad$ thus confirming that the system pointing stability is sufficient for demanding OPCPA work.

Additionally, the energy stability is just as important as the pointing stability, due to the exponential dependence of the gain in a OPCPA system on the pump intensity. The energy stability of this system was evaluated using a pyroelectric detector to sample the beam energy every 10th shot over an 8 hour workday. The result of this measurement is also shown in Figure 9-8 which shows a RMS fluctuation in the output power of 1% over 10 seconds and 3.5% over the full measurement period, which is acceptable for OPCPA pumping, Finally, we point out that this system has been in use for hundreds of hours since these upgrades were performed, with no measurable drop in performance. The only maintenance required has been regular service of the water chillers and slight alignment tuneups. There was only one incident which required major work on the system, which was the result of a fault whereby some outgassing occurred in the second multipass amplifier vacuum chamber, which necessitated opening the dewar and cleaning the crystal.

THIS PAGE INTENTIONALLY LEFT BLANK

Chapter 10

Conclusions

The field of ultrafast optics gives one the ability to peer into just about any physical process, being it macroscopic, chemical or even sub-atomic. In fact ultrafast lasers have been used to probe some of the smallest and shortest events that have even been observed. These abilities make ultrafast optics an incredibly important and productive field, with a huge amount of room to grow through the advancement of better laser sources and novel experiments to perform with them. In this work I present a first demonstration of a new technique–chirped pulse adiabatic difference frequency generation–for generating greater-than-octave spanning pulses in the mid-IR, which are both energetic and widely tunable. Furthermore, I propose that the technique pioneered with this work, and that of my colleagues, will enable experiments previously thought impossible by providing the laser sources needed to perform the demanding spectroscopic and high-field experiments proposed in theoretical works. I also report on the first demonstration of a new optical material, CSP, as used in a OPA pumped by a femtosecond $2\mu m$ laser to generate octave-spanning sub-2-cycle pules at $6\mu m$ with microjoule energies[40][40]. Furthermore, I present a variety of additional laser sources with few-cycle optical durations and peak intensities approaching a terawatt, which have already enabled a number of studies to interrogate the properties of gases and dielectrics under extreme electric fields[42][43][41][39] and generate coherent x-rays with photon energy approaching 500eV [27][61][61]. Finally, all of these sources are based on OPA/OPCPA techniques which are widely scalable both in repetition

rate and pulse energy, so all of these sources have clear paths for even higher average and peak powers.

Bibliography

[1] Giedrius Andriukaitis, Tadas Balciunas, Skirmantas Alisauskas, Audrius Pug-zlys, Andrius Baltuska, Tenio Popmintchev, Ming-Chang Chen, Margaret M. Murnane, and Henry C. Kapteyn. 90 GW peak power few-cycle mid-infrared pulses from an optical parametric amplifier. *Optics Letters*, 36(15):2755–2757, August 2011.

[2] J. A. Armstrong, N. Bloembergen, J. Ducuing, and P. S. Pershan. Interactions between Light Waves in a Nonlinear Dielectric. *Physical Review*, 127(6):1918–1939, September 1962.

[3] A. B. Arons and M. B. Peppard. Einstein's Proposal of the Photon Concept-a Translation of the Annalen der Physik Paper of 1905. *American Journal of Physics*, 33:367–374, May 1965.

[4] Satoshi Ashihara, Takahiro Mochizuki, Shunsuke Yamamoto, Tsutomu Shimura, and Kazuo Kuroda. Generation of Sub 50-fs Mid-Infrared Pulses by Optical Parametric Amplifier Based on Periodically-Poled MgO:LiNbO3. *Japanese Journal of Applied Physics*, 48(4R):042501, April 2009.

[5] N B Baranova, M A Bolshtyanskii, and Boris Ya Zel'dovich. Adiabatic energy transfer from a pump wave to its second harmonic. *Quantum Electronics*, 25(7):638–640, July 1995.

[6] Cosmin I. Blaga, Junliang Xu, Anthony D. DiChiara, Emily Sistrunk, Kaikai Zhang, Pierre Agostini, Terry A. Miller, Louis F. DiMauro, and C. D. Lin. Imaging ultrafast molecular dynamics with laser-induced electron diffraction. *Nature*, 483(7388):194–197, March 2012.

[7] Robert W. Boyd. *Nonlinear Optics*. Acad. Press, 2 edition, 2003.

[8] Scott H. Brewer and Stefan Franzen. Indium Tin Oxide Plasma Frequency Dependence on Sheet Resistance and Surface Adlayers Determined by Reflectance FTIR Spectroscopy. *The Journal of Physical Chemistry B*, 106(50):12986–12992, December 2002.

[9] D. Brida, M. Marangoni, C. Manzoni, S. De Silvestri, and G. Cerullo. Two-optical-cycle pulses in the mid-infrared from an optical parametric amplifier. *Optics Letters*, 33(24):2901–2903, December 2008.

[10] J. Bromage, J. Rothhardt, S. Haedrich, C. Dorrer, C. Jocher, S. Demmler, J. Limpert, A. Tunnermann, and J. D. Zuegel. Analysis and suppression of parasitic processes in noncollinear optical parametric amplifiers. *Optics Express*, 19(18):16797, August 2011.

[11] David Burghoff, Tsung-Yu Kao, Ningren Han, Chun Wang Ivan Chan, Xiaowei Cai, Yang Yang, Darren J. Hayton, Jian-Rong Gao, John L. Reno, and Qing Hu. Terahertz laser frequency combs. *Nature Photonics*, 8(6):462–467, June 2014.

[12] Chun-Lin Chang, Peter Krogen, Houkun Liang, Gregory J. Stein, Jeffrey Moses, Chien-Jen Lai, Jonathas P. Siqueira, Luis E. Zapata, F. X. Kaertner, and Kyung-Han Hong. Multi-mJ, kHz, ps deep-ultraviolet source. *Optics Letters*, 40(4):665, February 2015.

[13] M.-C. Chen, P. Arpin, T. Popmintchev, M. Gerrity, B. Zhang, M. Seaberg, D. Popmintchev, M. M. Murnane, and H. C. Kapteyn. Bright, Coherent, Ultra-fast Soft X-Ray Harmonics Spanning the Water Window from a Tabletop Light Source. *Physical Review Letters*, 105(17):173901, October 2010.

[14] J. A. Cox, W. P. Putnam, A. Sell, A. Leitenstorfer, and F. X. Kaertner. Pulse synthesis in the single-cycle regime from independent mode-locked lasers using attosecond-precision feedback. *Optics Letters*, 37(17):3579, September 2012.

[15] Guangyu Fan, Tadas Balciunas, Tsuneto Kanai, Giedrius Andriukaitis, Bruno E. Schmidt, Francois Legare, and Andrius Baltuska. Mid-IR pulse post-compression in hollow-core waveguide. page HS4B.2. OSA, 2016.

[16] M. D. Fayer. Dynamics of Liquids, Molecules, and Proteins Measured with Ultrafast 2d IR Vibrational Echo Chemical Exchange Spectroscopy. *Annual Review of Physical Chemistry*, 60(1):21–38, 2009.

[17] C. J. Fecko, J. J. Loparo, and A. Tokmakoff. Generation of 45 femtosecond pulses at 3 um with a KNbO3 optical parametric amplifier. *Optics Communications*, 241(4-6):521–528, November 2004.

[18] Michael Forster, C. Manzoni, S. Kaiser, Y. Tomioka, Y. Tokura, R. Merlin, and A. Cavalleri. Nonlinear phononics as an ultrafast route to lattice control. *Nature Physics*, 7(11):854–856, November 2011.

[19] P. A. Franken, A. E. Hill, C. W. Peters, and G. Weinreich. Generation of Optical Harmonics. *Physical Review Letters*, 7(4):118–119, August 1961.

[20] Erhard W. Gaul, Todd Ditmire, Mikael Martinez, Skyler Douglas, Dan Gorski, Watson Henderson, Greg R. Hays, Alvin Erlandson, John A. Caird, Igor Jovanovic, Chris Ebbers, and William Molander. Design of the Texas Petawatt Laser. In *Conference on Lasers and Electro-Optics/Quantum Electronics and Laser Science and Photonic Applications Systems Technologies (2005), paper JFB2*, page JFB2. Optical Society of America, May 2005.

[21] Rachel Glenn and Marcos Dantus. Single Broadband Phase-Shaped Pulse Stimulated Raman Spectroscopy for Standoff Trace Explosive Detection. *The Journal of Physical Chemistry Letters*, 7(1):117–125, January 2016.

[22] J. P. Gordon, H. J. Zeiger, and C. H. Townes. The Maser-New Type of Microwave Amplifier, Frequency Standard, and Spectrometer. *Physical Review*, 99(4):1264–1274, August 1955.

[23] H. A. Haus. Mode-locking of lasers. *IEEE Journal of Selected Topics in Quantum Electronics*, 6(6):1173–1185, November 2000.

[24] M. Hemmer, A. Thai, M. Baudisch, H. Ishizuki, T. Taira, and J. Biegert. 18-uJ energy, 160-kHz repetition rate, 250-MW peak power mid-IR OPCPA. *Chinese Optics Letters*, 11(1):013202, January 2013.

[25] Kyung-Han Hong, Chun-Lin Chang, Peter Krogen, Houkun Liang, Gregory J. Stein, Jeffrey Moses, Chien-Jen Lai, and Franz X. Kaertner. Multi-mJ, kHz picosecond deep UV source based on a frequency-quadrupled cryogenic Yb:YAG laser. volume 9513, pages 95130U–95130U–8, 2015.

[26] Kyung-Han Hong, Shu-Wei Huang, Jeffrey A. Moses, Xing Fu, Chien-Jen Lai, and Franz X. Kaertner. High-energy, Few-cycle, kHz OPCPA at 2.1 um Pumped by a Picosecond Cryogenic Yb:YAG Laser. In *CLEO:2011 - Laser Applications to Photonic Applications*, OSA Technical Digest (CD), page CTuT3. Optical Society of America, May 2011.

[27] Kyung-Han Hong, Chien-Jen Lai, Jonathas Siqueira, Peter Krogen, Jeffrey Moses, Martin Smrz, Luis E. Zapata, and F. X. Kaertner. Multi-mJ, kHz, 2.1-Îijm OPCPA for high-flux soft X-ray high-harmonic radiation. In *Research in Optical Sciences*, OSA Technical Digest (online), page JW2A.5. Optical Society of America, March 2014.

[28] Kyung-Han Hong, Aleem Siddiqui, Jeffrey Moses, Juliet Gopinath, John Hybl, F. Omer Ilday, Tso Yee Fan, and F. X. Kaertner. Generation of 287 W, 5.5 ps pulses at 78 MHz repetition rate from a cryogenically cooled Yb:YAG amplifier seeded by a fiber chirped-pulse amplification system. *Optics Letters*, 33(21):2473–2475, November 2008.

[29] Weiyi Hong, Peixiang Lu, Qianguang Li, and Qingbin Zhang. Broadband water window supercontinuum generation with a tailored mid-IR pulse in neutral media. *Optics Letters*, 34(14):2102, July 2009.

[30] Shu-Wei Huang, Giovanni Cirmi, Jeffrey Moses, Kyung-Han Hong, Siddharth Bhardwaj, Jonathan R. Birge, Li-Jin Chen, Irina V. Kabakova, Enbang Li, Benjamin J. Eggleton, Giulio Cerullo, and F. X. Kaertner. Optical waveform synthesizer and its application to high-harmonic generation. *Journal of Physics B: Atomic, Molecular and Optical Physics*, 45(7):074009, April 2012.

[31] Shu-Wei Huang, Giovanni Cirmi, Jeffrey Moses, Kyung-Han Hong, Siddharth Bhardwaj, Jonathan R. Birge, Li-Jin Chen, Enbang Li, Benjamin J. Eggleton, Giulio Cerullo, and Franz X. Kaertner. High-energy pulse synthesis with sub-cycle waveform control for strong-field physics. *Nat Photon*, 5(8):475–479, August 2011.

[32] Cheng Jin, Kyung-Han Hong, and C. D. Lin. Optimal generation of high harmonics in the water-window region by synthesizing 800-nm and mid-infrared laser pulses. *Optics Letters*, 40(16):3754, August 2015.

[33] D. Kartashov, S. Alisauskas, Audrius Pugzlys, A. Voronin, A. Zheltikov, M. Petrarca, Pierre Bejot, J. Kasparian, J.-P. Wolf, and A. Baltuska. Mid-infrared laser filamentation in molecular gases. *Optics Letters*, 38(16):3194, August 2013.

[34] Vincent Kemlin, Benoit Boulanger, Valentin Petrov, Patricia Segonds, B. Mãĭnaert, Peter G. Schunneman, and Kevin T. Zawilski. Nonlinear, dispersive, and phase-matching properties of the new chalcopyrite CdSiP_2 [Invited]. *Optical Materials Express*, 1(7):1292, November 2011.

[35] I. J. Kim, H. T. Kim, C. M. Kim, J. J. Park, Y. S. Lee, K.-H. Hong, and C. H. Nam. Efficient high-order harmonic generation in a two-color laser field. *Applied Physics B*, 78(7-8):859–861, April 2004.

[36] Peter Krogen, Haim Suchowski, Houkun Liang, F. X. Kaertner, and Jeffrey Moses. Toward Multi-Octave Pulse Shaping by Adiabatic Frequency Conversion. In *CLEO: Science and Innovations*, pages SW1O–3. Optical Society of America, 2015.

[37] Peter Krogen, Haim Suchowski, Gregory J. Stein, F. X. Kaertner, and Jeffrey Moses. Tunable and Near-Fourier-limited Few-Cycle Mid-IR Pulses via an Adiabatically Chirped Difference Frequency Grating. page SM3I.5. OSA, 2014.

[38] T. Lang, A. Harth, J. Matyschok, T. Binhammer, M. Schultze, and U. Morgner. Impact of temporal, spatial and cascaded effects on the pulse formation in ultra-broadband parametric amplifiers. *Optics Express*, 21(1):949, January 2013.

[39] Hou Kun Liang, Peter Krogen, Darshana Weerawarne, Chien-Jen Lai, Rostislav Grynko, Bonggu Shim, F. X. Kaertner, and Kyung-Han Hong. Mid-IR Laser Filamentation in air at a kHz Repetition Rate. In *Mid-Infrared Coherent Sources*, pages MT2C–5. Optical Society of America, 2016.

[40] Hou Kun Liang, Peter Krogen, K. Zawilski, Peter G. Schunemann, Tino Lang, Uwe Morgner, F. X. Kaertner, Jeffrey Moses, and Kyung-Han Hong. Octave-Spanning 6-um OPA Pumped by 2.1-um OPCPA. In *Mid-Infrared Coherent Sources*, pages MS4C–1. Optical Society of America, 2016.

[41] Hou Kun Liang, Peter R. Krogen, Ross Grynko, Ondrej Novak, Chun-Lin L. Chang, Gregory J. Stein, Darshana Weerawarne, Bonggu Shim, Franz Kaernter, and Kyung-Han Hong. Mid-IR Filamentation in Dielectrics: 3-octave-spanning Supercontinuum Generation and Sub-2-cycle Self-compression. In *CLEO: QELS_Fundamental Science*, pages FTu4D–2. Optical Society of America, 2015.

[42] Houkun Liang, Peter Krogen, Ross Grynko, Ondrej Novak, Chun-Lin Chang, Gregory J. Stein, Darshana Weerawarne, Bonggu Shim, F. X. Kaertner, and Kyung-Han Hong. Three-octave-spanning supercontinuum generation and sub-two-cycle self-compression of mid-infrared filaments in dielectrics. *Optics Letters*, 40(6):1069–1072, 2015.

[43] Houkun Liang, Peter R. Krogen, Ross Grynko, Ondrej Novak, Chun-Lin L. Chang, Gregory J. Stein, Darshana Weerawarne, Bonggu Shim, F. X. Kaertner, and Kyung-Han Hong. 3-octave Supercontinuum Generation and Sub-2-cycle Self-compression of Mid-IR Filaments in Dielectrics. In *Advanced Solid State Lasers*, pages ATu5A–4. Optical Society of America, 2014.

[44] LIGO Scientific Collaboration and Virgo Collaboration. Observation of Gravitational Waves from a Binary Black Hole Merger. *Physical Review Letters*, 116(6):061102, February 2016.

[45] T. H. Maiman. Stimulated Optical Radiation in Ruby. *Nature*, 187(4736):493–494, August 1960.

[46] J. Clerk Maxwell. A Dynamical Theory of the Electromagnetic Field. *Philosophical Transactions of the Royal Society of London*, 155:459–512, January 1865.

[47] B. W. Mayer, C. R. Phillips, L. Gallmann, M. M. Fejer, and U. Keller. Sub-four-cycle laser pulses directly from a high-repetition-rate optical parametric chirped-pulse amplifier at 3.4um. *Optics Letters*, 38(21):4265–4268, November 2013.

[48] Randy D. Mehlenbacher, Thomas J. McDonough, Maksim Grechko, Meng-Yin Wu, Michael S. Arnold, and Martin T. Zanni. Energy transfer pathways in semiconducting carbon nanotubes revealed using two-dimensional white-light spectroscopy. *Nature Communications*, 6:6732, 2015.

[49] J. Moses, S.-W. Huang, K.-H. Hong, O. D. Mucke, E. L. Falcao-Filho, A. Benedick, F. O. Ilday, A. Dergachev, J. A. Bolger, B. J. Eggleton, and F. X. Kaertner. Highly stable ultrabroadband mid-IR optical parametric chirped-pulse amplifier optimized for superfluorescence suppression. *Optics Letters*, 34(11):1639–1641, June 2009.

[50] Jeffrey Moses and Shu-Wei Huang. Conformal profile theory for performance scaling of ultrabroadband optical parametric chirped pulse amplification. *Journal of the Optical Society of America B*, 28(4):812–831, April 2011.

[51] Jeffrey Moses, Cristian Manzoni, Shu-Wei Huang, Giulio Cerullo, and Franz X. Kaertner. Temporal optimization ofultrabroadband high-energy OPCPA. *Optics Express*, 17(7):5540–5555, March 2009.

[52] Yutaka Nomura, Hideto Shirai, Kenta Ishii, Noriaki Tsurumachi, Alexander A. Voronin, Aleksei M. Zheltikov, and Takao Fuji. Phase-stable subcycle mid-infrared conical emission from filamentation in gases. *Optics Express*, 20(22):24741–24747, October 2012.

[53] Poul B. Petersen and Andrei Tokmakoff. Source for ultrafast continuum infrared and terahertz radiation. *Optics Letters*, 35(12):1962–1964, June 2010.

[54] C. R. Phillips, B. W. Mayer, L. Gallmann, M. M. Fejer, and U. Keller. Design constraints of optical parametric chirped pulse amplification based on chirped quasi-phase-matching gratings. *Optics Express*, 22(8):9627, April 2014.

[55] T. Popmintchev, M.-C. Chen, D. Popmintchev, P. Arpin, S. Brown, S. Alisauskas, G. Andriukaitis, T. Balciunas, O. D. Mucke, A. Pugzlys, A. Baltuska, B. Shim, S. E. Schrauth, A. Gaeta, C. Hernandez-Garcia, L. Plaja, A. Becker, A. Jaron-Becker, M. M. Murnane, and H. C. Kapteyn. Bright Coherent Ultrahigh Harmonics in the keV X-ray Regime from Mid-Infrared Femtosecond Lasers. *Science*, 336(6086):1287–1291, June 2012.

[56] Audrius Pugzlys, V Shumakova, P Malevich, Tsuneto Kanai, S Alisauskas, Giedrius Andriukaitis, Edgar Kaksis, T Balciunas, Guangyu Fan, A Voronin, A M. Zheltikov, D Faccio, D Kartashov, and Andrius Baltuska. Multi-millijoule Few-Optical-Cycle Pulses in Mid-IR: Scaling Power, Energy and Wavelength. page AM3A.1. OSA, 2015.

[57] D. J. Ripin, J. R. Ochoa, R. L. Aggarwal, and T. Y. Fan. 300-W cryogenically cooled Yb:YAG laser. *IEEE Journal of Quantum Electronics*, 41(10):1274–1277, October 2005.

[58] D. Sanchez, M. Hemmer, M. Baudisch, S. L. Cousin, K. Zawilski, P. Schunemann, O. Chalus, C. Simon-Boisson, and J. Biegert. 7 Îijm, ultrafast, sub-millijoule-level mid-infrared optical parametric chirped pulse amplifier pumped at 2 um. *Optica*, 3(2):147, February 2016.

[59] G. Sansone, F. Kelkensberg, J. F. Perez-Torres, F. Morales, M. F. Kling, W. Siu, O. Ghafur, P. Johnsson, M. Swoboda, E. Benedetti, F. Ferrari, F. Lepine, J. L. Sanz-Vicario, S. Zherebtsov, I. Znakovskaya, A. LâĂŹHuillier, M. Yu Ivanov, M. Nisoli, F. Martin, and M. J. J. Vrakking. Electron localization following attosecond molecular photoionization. *Nature*, 465(7299):763–766, June 2010.

[60] Alexander Sell, Rudiger Scheu, Alfred Leitenstorfer, and Rupert Huber. Field-resolved detection of phase-locked infrared transients from a compact Er:fiber system tunable between 55 and 107 THz. *Applied Physics Letters*, 93(25):251107, December 2008.

[61] Gregory J. Stein, Chien-Jen Lai, Phillip D. Keathley, Peter R. Krogen, Houkun Liang, Chun-Lin L. Chang, Kyung-Han Hong, Guillaume Laurent, and Franz X. Kaertner. Versatile Simulation Package for Ultrafast Pulse Propagation and High Harmonic Generation. page JW2A.36. OSA, 2015.

[62] Haim Suchowski, Peter R. Krogen, Shu-Wei Huang, Franz X. Kaertner, and Jeffrey Moses. Octave-spanning coherent mid-IR generation via adiabatic difference frequency conversion. *Optics Express*, 21(23):28892–28901, November 2013.

[63] Haim Suchowski, Dan Oron, Ady Arie, and Yaron Silberberg. Geometrical representation of sum frequency generation and adiabatic frequency conversion. *Physical Review A*, 78(6):063821, December 2008.

[64] Haim Suchowski, Gil Porat, and Ady Arie. Adiabatic processes in frequency conversion. *Laser & Photonics Reviews*, 8(3):333–367, May 2014.

[65] Michael E. Swanwick, Phillip D. Keathley, Arya Fallahi, Peter R. Krogen, Guillaume Laurent, Jeffrey Moses, F. X. Kaertner, and Luis F. VelÃ¡squez-GarcÃa. Nanostructured ultrafast silicon-tip optical field-emitter arrays. *Nano letters*, 14(9):5035–5043, 2014.

[66] Eiko Takaoka and Kiyoshi Kato. Temperature Phase-Matching Properties for Harmonic Generation in GaSe. *Japanese Journal of Applied Physics*, 38(Part 1, No. 5A):2755–2759, May 1999.

[67] I. Thomann, A. Bahabad, X. Liu, R. Trebino, M. M. Murnane, and H. C. Kapteyn. Characterizing isolated attosecond pulses from hollow-core waveguides using multi-cycle driving pulses. *Optics Express*, 17(6):4611, March 2009.

[68] Rick Trebino, Kenneth W. DeLong, David N. Fittinghoff, John N. Sweetser, Marco A. KrumbÃ¼gel, Bruce A. Richman, and Daniel J. Kane. Measuring ultrashort laser pulses in the time-frequency domain using frequency-resolved optical gating. *Review of Scientific Instruments*, 68(9):3277–3295, September 1997.

[69] J. Ward, E. Schlecht, G. Chattopadhyay, A. Maestrini, J. Gill, F. Maiwald, H. Javadi, and I. Mehdi. Capability of THz sources based on Schottky diode frequency multiplier chains. In *Microwave Symposium Digest, 2004 IEEE MTT-S International*, volume 3, pages 1587–1590 Vol.3, June 2004.

[70] Pengfei Wei, Jing Miao, Zhinan Zeng, Chuang Li, Xiaochun Ge, Ruxin Li, and Zhizhan Xu. Selective Enhancement of a Single Harmonic Emission in a Driving Laser Field with Subcycle Waveform Control. *Physical Review Letters*, 110(23):233903, June 2013.

[71] A. Wirth, M. Th Hassan, I. Grguras, J. Gagnon, A. Moulet, T. T. Luu, S. Pabst, R. Santra, Z. A. Alahmed, A. M. Azzeer, V. S. Yakovlev, V. Pervak, F. Krausz, and E. Goulielmakis. Synthesized Light Transients. *Science*, 334(6053):195–200, October 2011.

[72] Clarence Zener. Non-Adiabatic Crossing of Energy Levels. *Proceedings of the Royal Society of London. Series A*, 137(833):696–702, September 1932.